Supplemental Information

Coordination engineering with crown ethers for perovskite precursor stabilization and universal defect passivation

Zhongyang Zhang [a], Yuxuan Yang [b], Zijian Huang [c], Qiaoling Xu [d,e], Siyuan Zhu [d,f], Minghua Li [g], Peng Zhao [b], Hong Cui [b], Sihan Li [b], Xi Jin [d], Xiaoxue Wu [d], Mingyue Han [d], Yu Zhang [d], Ningjiu Zhao [d], Chao Zou [d], Qijie Liang [d], Lede Xian [d,h], Jinsong Hu [i], Cheng Zhu [a], Yihua Chen [a], Yang Bai [a], Yujing Li [a], Qi Chen [a], Huanping Zhou [c], Bao Zhang *[b], Yan Jiang *[a]

[a] School of Materials Science and Engineering, Beijing Institute of Technology, Beijing 100081, China
E-mail: yan.jiang@bit.edu.cn (Yan Jiang).

[b] School of Chemical Engineering and Technology, Tianjin University, Tianjin 300350, China
E-mail: baozhang@tju.edu.cn (Bao Zhang)

[c] School of Materials Science and Engineering, Peking University, Beijing 100091, China

[d] Songshan Lake Materials Laboratory, Dongguan, Guangdong 523808, China

[e] College of Physics and Electronic Engineering, Center for Computational Sciences, Sichuan Normal University, Chengdu 610068, China

[f] Department of Physics, Liaoning University, Shenyang 110036, China

[g] College of Chemical Engineering, Beijing Advanced Innovation Center for Soft Matter Science and Engineering, Beijing University of Chemical Technology, Beijing 100029, China

[h] Max Planck Institute for the Structure and Dynamics of Matter, Center for Free Electron Laser Science, Hamburg, 22761, Germany

[i] Beijing National Laboratory for Molecular Sciences (BNLMS), Institute of Chemistry, Chinese Academy of Sciences, Beijing 100190, China

This file includes:

Methods

Figure S1 to 47

Note S1 to 14

Table S1 to 11

References

Methods

Materials:

Pre-patterned ITO glass substrates were purchased from Advanced Election Technology Co., Ltd. Chlorobenzene (CB), N,N-dimethylformamide (DMF), dimethyl sulfoxide (DMSO), acetonitrile (ACN), isopropanol (IPA), cesium iodide (CsI), lead bromide ($PbBr_2$), formamidine acetate (FAAc), 4-tert-butylpyridine (tBP) and bis(trifluoromethane)sulfonimide lithium salt (Li-TFSI) were purchased from Sigma-Aldrich. Formamidinium iodide (FAI), methylammonium chloride (MACl), formamidinium bromide (FABr) and methylammonium bromide (MABr) were purchased from Greatcell Solar. Lead iodide (PbI_2) was purchased from TCI. Lead chloride ($PbCl_2$), Spiro-OMeTAD, PTAA, $PC_{61}BM$, and 2-phenylethylamine hydroiodide (PEAI) were purchased from Xi'an Polymer Light Technology. Tin (IV) oxide (SnO_2) colloidal solution (15% in H_2O) was purchased from Alfa Aesar. 18-crown-6 (18C6), 15-crown-5 (15C5), 1-aza-18-crown-6-ether (A18C6), 4,13-diaza-18-crown-6-ether (DA18C6), 1-aza-15-crown-5-ether (A15C5), 1,7-diaza-15-crown 5-ether (DA15C5), hydriodic acid (HI, 55-57 wt.% in H_2O, with 1.5% hypophosphorous acid), 2-hydroxy-4-methoxy-5-sulfonate-benzophenone (SBP) and γ-butyrolactone (GBL) were purchased from Aladdin.

Synthesis of $FAPbI_3$ and $MAPbBr_3$ single crystals:

Firstly, formamidinium iodide (FAI) was synthesized by reacting 6 mL of hydroiodic acid (55-57 wt.% in water) with 3.9 g of formamidinium acetate (FAAc) in an ice bath for 2 hours. The light yellow mixture was evaporated at 100 °C for 1 h to remove HAc and remaining HI, and the white precipitate was recovered. The crude product was recrystallized in hot anhydrous ethanol and the white platelike crystal was obtained. Then the white crystal was washed with diethyl ether and dried.

Single crystal $FAPbI_3$ was synthesized referring to the method described elsewhere[1]. 2.2 g of synthesized FAI, 6.0 g of PbI_2 and 10 mL of GBL were mixed in a closed glass bottle (volume with 20 mL capacity). The yellow solution was filtered by

0.45 μm nylon filters and heated on a hot plate (60 ℃ for 1 h, 110 ℃ for 1 h, 130 ℃ for 1 h and 150 °C for 2 h). The shiny black single crystals (α-$FAPbI_3$) were grown in GBL solution, dried on a hot plate at 110 °C for 2 h in a nitrogen glove box and stored in transparent glass bottles (the yield of $FAPbI_3$ was ~30%)[53]. The phase purity of $FAPbI_3$ was verified by XRD.

Single crystal $MAPbBr_3$ was synthesized referring to the literature[2]. 2.4 g of MABr, 7.7 g of $PbBr_2$, and 15 mL of DMF were mixed in a closed glass bottle and stirred overnight at room temperature (20 ℃). After complete dissolution, the colorless solution was filtered by 0.45 μm filters, moved to a 30 mL glass bottle, and heated on a hot plate (40 ℃ for 1 h, 70 ℃ for 1 h, 100 ℃ for 1 h, 110 °C for 1 h and 120 °C for 1 h). The bright orange nanocubes ($MAPbBr_3$) were grown in DMF solution, dried on a hot plate at 80 °C for 2 h in a nitrogen glove box and collected in transparent glass bottles (the yield of $MAPbBr_3$ was ~50%). The phase purity of $MAPbBr_3$ was verified by XRD.

Precursor Preparation:

Perovskite precursor solutions were prepared in a nitrogen glove box. For 1.56 eV [$Cs_{0.04}(FA_{0.97}MA_{0.03})_{0.96}Pb(I_{0.97}Br_{0.03})_3$] perovskite[25], undoped perovskite precursor solution was prepared by dissolving 0.068 mol/L CsI, 0.044 mol/L MABr, 0.444 mol/L MACl, 0.044 mol/L $PbBr_2$, 1.465 mol/L FAI and 1.594 mol/L PbI_2 in a mixed anhydrous solvent (DMF:DMSO=4:1). For 1.52 eV [$(FAPbI_3)_{0.95}(MAPbBr_3)_{0.05}$] perovskite[3], undoped perovskite precursor solution was prepared by dissolving 0.069 mol/L MABr, 0.069 mol/L $PbBr_2$, 0.489 mol/L MACl, 1.40 mol/L FAI and 1.40 mol/L PbI_2 in a mixed anhydrous solvent (DMF:DMSO=4:1). For 1.67 eV [$Cs_{0.22}FA_{0.78}Pb(I_{0.85}Br_{0.15})_3-0.03MAPbCl_3$] wide bandgap perovskite[4], undoped perovskite precursor solution was prepared by dissolving 0.045 mol/L MACl, 0.045 mol/L $PbCl_2$, 0.33 mol/L CsI, 0.225 mol/L FABr, 0.225 mol/L $PbBr_2$, 0.945 mol/L FAI and 1.29 mol/L PbI_2 in a mixed anhydrous solvent (DMF:DMSO=4:1).

The ACE stock solutions (4 mmol/L) were prepared in a mixed solvent (DMF:DMSO=4:1). For the ACE-doped perovskite precursor solution, the

corresponding amount of the ACE solution was added to the undoped perovskite precursor solution, followed by stirring at 60 ℃ for 1 hour and cooling down before use. The PEAI solution (20 mmol/L) was obtained by dissolving PEAI powder in IPA. Lastly, 72.3 mg of spiro-OMeTAD, 28.5 μL of tBP and 17.5 μL of Li-TFSI (520 mg/mL in acetonitrile) were mixed in 1 mL CB. All of the solutions were filtered by 0.22 μm filters before use.

Device fabrication:

Pre-patterned ITO glass substrates were cleaned with anhydrous alcohol and acetone using an ultrasonic cleaner. To prepare SnO_2 thin film, 100 μL SnO_2 colloidal solution was spin-coated onto the cleaned ITO substrate at 4000 rpm for 30 s, followed by drying at 150 °C for 30 min in air. Perovskite precursor solutions were spin-coated onto the SnO_2 layer at 6000 rpm for 30 s in a dry air glove box (RH<5%). During the spin-coating process, ~200 μL chlorobenzene was rapidly dropped onto the substrates at 22 s. The films were heated at 100 ℃ for 30 min in a dry air glove box, and then the samples were transferred to a nitrogen glove box. For 1.56 eV perovskite, 50 μL PEAI solution was spin-coated onto perovskite films at 5000 rpm for 30 s without additional thermal annealing. The spiro-OMeTAD solution was deposited on the as-prepared perovskite substrates at 3000 rpm for 30 s. Finally, 50 nm Au electrode was thermally evaporated under a high vacuum condition ($<10^{-5}$ Pa).

For high-efficiency 1.56 eV PSCs, in order to enhance phase purity of cubic α-$FAPbI_3$ and reduce defects[5], the conventional precursor mixture (FAI, PbI_2, MABr and $PbBr_2$) was replaced with our home-made presynthesized single crystals. Specifically, 0.068 mol/L CsI, 0.13 mol/L PbI_2, 0.444 mol/L MACl, 0.044 mol/L $MAPbBr_3$ and 1.465 mol/L $FAPbI_3$ were dissolved in a mixed anhydrous solvent (DMF:DMSO=4:1) for preparing perovskite solution. Then the corresponding amount of the A18C6 was added according to the method above. Other fabrication processes were not changed.

For the operational stability tests, the devices with a structure of ITO/SnO_2/PVK/PEAI/HTL/MoO_3/Au were fabricated. For preparing SnO_2 layer, 2-hydroxy-4-methoxy-5-sulfonate-benzophenone was added into SnO_2 solution (0.5

mg/mL) to passivate interface defects. The SnO_2 solution was filtered by 0.45 μm filters before use, and 150 μL solution was spin-coated onto the ITO substrate at 4000 rpm for 30 s, followed by drying at 90 °C for 5 min and 150 °C for 30 min. For preparing $[Cs_{0.04}(FA_{0.97}MA_{0.03})_{0.96}Pb(I_{0.97}Br_{0.03})_3]$ perovskite solution, presynthesized $FAPbI_3$ and $MAPbBr_3$ single crystals were used to replace FAI, PbI_2, MABr and $PbBr_2$ as discussed above. 75 μL PEAI solution (20 mmol/L) was spin-coated onto perovskite films at 5000 rpm for 30 s, followed by drying at 100 °C for 5 min. PTAA/spiro-OMeTAD was used as hole transport layer[50]. The PTAA solution (10 mg/mL PTAA in CB, containing 10 μL of tBP and 5 μL of Li-TFSI) and the spiro-OMeTAD solution (72.3 mg/mL spiro-OMeTAD in CB, containing 28.5 μL of tBP and 17.5 μL of Li-TFSI) were mixed in equal volumes. Then 50 μL mixed solution was deposited onto the PEAI-coated perovskite layer at 3000 rpm for 30 s. 10 nm MoO_3 and 200 nm Au were thermally evaporated under a high vacuum condition.

Characterization:

Liquid-state ^1H NMR spectra were measured by using the Varian Inova 400. UV-vis absorption spectra were measured by using HITACHI UH4150. The DLS colloid size distributions were obtained by Malvern Zetasizer Nano Series spectrophotometer. XPS characterizations were performed by using Thermo Fisher ESCALAB Xi+ (Al Kα source). XRD patterns were measured by using a Bruker D8 Advance X-ray diffractometer (Cu Kα radiation). The Grazing incidence wide-angle X-ray scattering (GIWAXS) data were obtained at beamline BL14B1 of the Shanghai Synchrotron Radiation Facility (SSRF) using X-ray with a wavelength of 1.243 Å. FE-SEM images were obtained by using the Zeiss Gemini SEM 300. AFM topography were obtained by Asylum Research Cypher S (Oxford). PL mapping was obtained by Confocal Microscopy (SPCM-1000) supported by Enli Technology Co., Ltd. Steady-state PL spectra were tested by using HITACHI F-7100 and excited by a 470-nm light source of a Xe lamp with a 550-nm filter. Time-resolved photoluminescence spectra were recorded by Light Conversion Harpia with an excitation of 470 nm. For light intensity-dependent open-circuit voltage measurements, neutral density filters (Thorlabs) were

used for reducing light intensity. Mott-Schottky plots were obtained by an electrochemical workstation (CHI 660E). For the space-charge-limited-current (SCLC) test, the trap-state densities of devices were evaluated by dark *J-V* characteristics of a hole-only device (ITO/PTAA/PVK/spiro-OMeTAD/Au) and an electron-only device (ITO/SnO_2/PVK/$PC_{61}BM$/Au). The *J-V* characteristics of photovoltaic devices were measured with a solar simulator (Newport) and Keithley 2400 source meter under AM 1.5 G standard irradiation (1000 W/m^2) in an ambient air atmosphere (25 ℃, RH 30%). Intensity of the solar simulator was calibrated using a certified monocrystalline silicon solar cell (KG5). The active area of device is 0.08313 cm^2, defined by a metal mask. Both reverse scans (1.2 → 0 V, step: 0.02 V, delay time: 20 ms) and forward scans (0 → 1.2 V, step: 0.02 V, delay time: 20 ms) were conducted. External quantum efficiency (EQE) is recorded on a solar cell quantum efficiency measurement system (QE-R) supported by Enli Technology. A calibrated Si diode with a known spectral response is used as a reference. For the operational tests, the unencapsulated devices with the structure of ITO/SnO_2/PVK/PEAI/HTL/MoO_3/Au were tested under 100 mW/cm^2 at 25 ℃ in nitrogen, and the PSCs were aged under a large area white LED lamp and at their maximum power points (MPP).

DFT calculation:

The highest occupied molecular orbital (HOMO) and lowest unoccupied molecular orbital (LUMO) energy levels of molecules were calculated using the Gaussian 09 package. At the same calculation level, the ground state structure optimization and vibration analysis were carried out based on the B3LYP functional and the def2TZVP basis set, respectively, to ensure that the molecule is located at the lowest point of potential energy. In the Multiwfn program[6], the positions and distributions of the HOMO and LUMO energy levels were obtained. The electrostatic potential map was evaluated with the code Multiwfn, which was based on the highly effective algorithm.

The Vienna Ab initio simulation package (VASP) was used to determine the ground state of the system[7]. The electron-ion interaction was described by using projector

augmented-wave (PAW) pseudopotentials. The exchange-correlation functionals were treated at the general gradient approximation (GGA) level with the method of Perdew, Burke, and Ernzerhof (PBE)[8]. The $FAPbI_3$ (001) PbI_2-terminated surface slab model was built based on the cubic-phased $2\sqrt{2} \times 2\sqrt{2}$ supercells containing 7 atomic layers. DFT was most conveniently set up using periodic boundary condition and therefore, an auxiliary vacuum region at least 25 Å along the z-direction was added. This region was chosen to be large enough such that artificial interactions between periodic slabs could be neglected. An energy cutoff of 500 eV for the plane wave expansion and a k-point mesh of 1×1×1 were used for all subsequent calculations. The convergence of total energy reached the level of less than 1.0×10^{-5} eV, and the residual forces on the relaxed atoms became smaller than 0.05 eV/Å. Long-range dispersion interactions, which played an important role on organic cation orientation and structural optimization[9], were considered in this work. The van der Waals correction proposed by the Grimme potential (D3-BJ) was employed for all subsequent calculations[10]. The bottom 4 layers of atoms were fixed and all other atoms were fully relaxed during structural optimization. To ensure computational efficiency in the simulation, LREAL = A has been adopted, and parallel computing parameters such as NSIM have been set appropriately. In the ionic relaxation of the slab model, ISIF = 2 has been employed. The charge density difference distribution was defined as $\Delta\rho = \rho$ (total) - ρ (PVK slab) - ρ (molecule), where ρ (total) was the total charge density of the slab after the perovskite-molecule interactions, ρ (PVK) and ρ (molecule) were the charge densities of the isolated perovskite slab and the molecule, respectively. Structure visualization and 3D charge density difference plotting were performed by the VESTA. VASPKIT was used for plotting the planar average charge density difference[11].

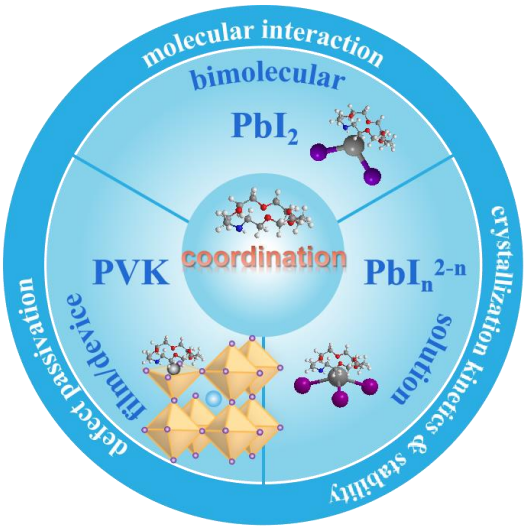

Figure S1. Schematic diagram of the coordination ability of crown ethers and the interactions with PbI_2, iodoplumbates solution and perovskite film.

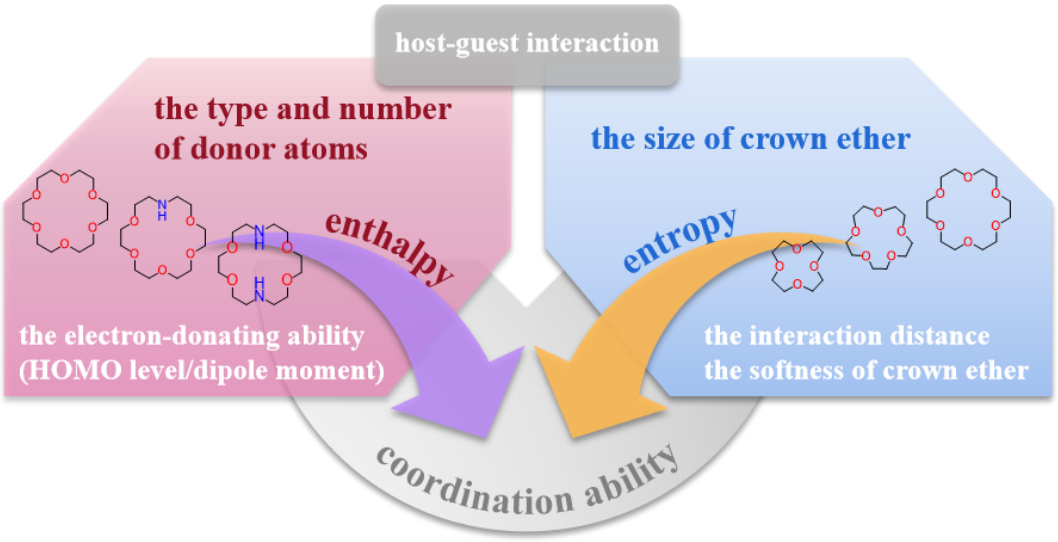

Figure S2. Schematic diagram of influencing factors for coordination ability based on host-guest interaction.

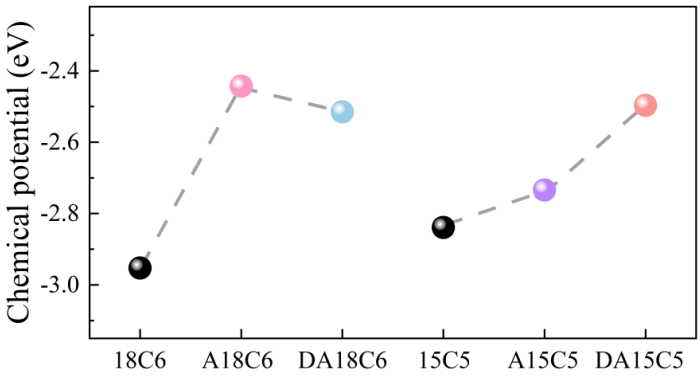

Figure S3. The energy values of chemical potential (μ) of crown ethers.

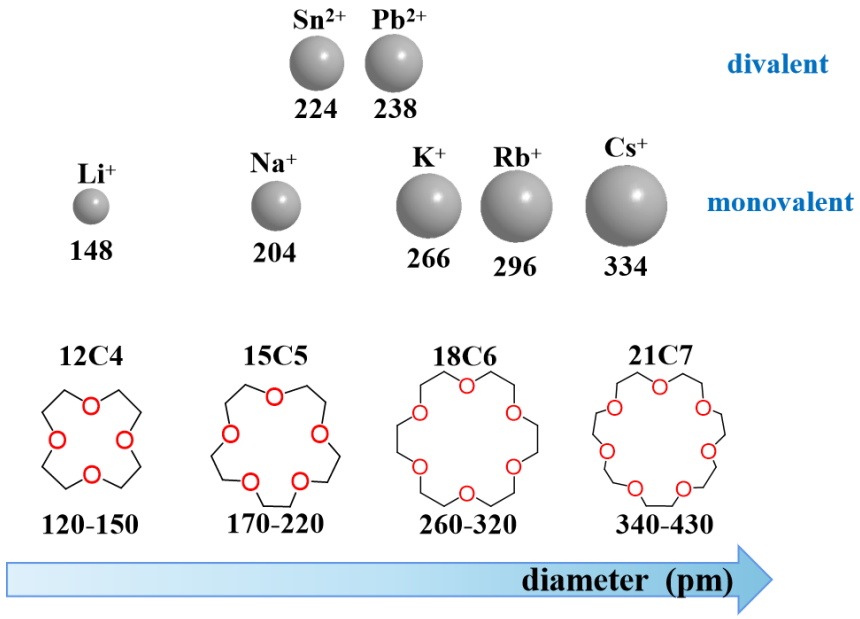

Figure S4. Schematic diagram of diameters of cations and cavity sizes of crown ethers. 12C4, 15C5, 18C6 and 21C7 are abbreviations for 12-crown-4 (12C4), 15-crown-5 (15C5), 18-crown-6 (18C6) and 21-crown-7 (21C7)[12,13].

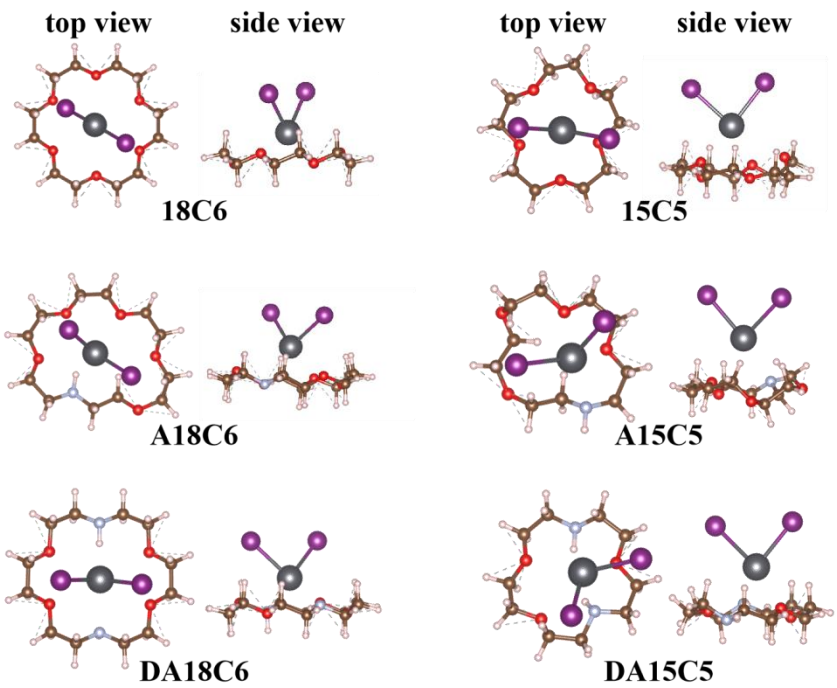

Figure S5. Top and side views of the atomic structure of crown ethers interacting with PbI_2 used in the DFT calculation. The brown, white, red, ice-blue, gray and purple colors indicate C, H, O, N, Pb and I atoms respectively.

A18C6

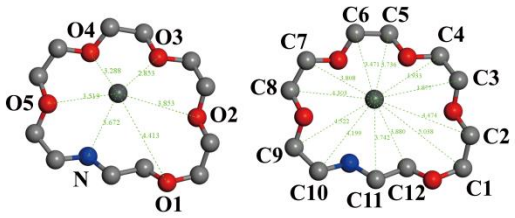

atom	Distance (Å)	atom	Distance (Å)	atom	Distance (Å)
O1	4.413	C1	5.038	C7	3.808
O2	3.853	C2	4.474	C8	4.303
O3	2.853	C3	3.877	C9	4.522
O4	3.288	C4	3.933	C10	4.199
O5	3.519	C5	3.736	C11	3.742
N	3.672	C6	3.471	C12	3.880

DA18C6

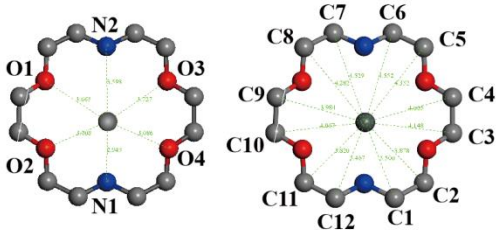

atom	Distance (Å)	atom	Distance (Å)	atom	Distance (Å)
O1	3.665	C1	3.500	C7	4.529
O2	3.008	C2	3.878	C8	4.282
O3	3.727	C3	4.148	C9	3.984
O4	3.086	C4	4.065	C10	4.067
N1	2.949	C5	4.332	C11	3.820
N2	3.598	C6	4.552	C12	3.467

A15C5

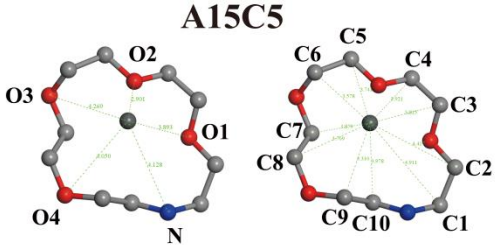

atom	Distance (Å)	atom	Distance (Å)	atom	Distance (Å)
O1	3.893	C1	4.911	C6	3.578
O2	2.901	C2	4.417	C7	3.879
O3	4.269	C3	3.815	C8	3.709
O4	4.050	C4	3.921	C9	3.310
N	4.128	C5	3.471	C10	3.978

DA15C5

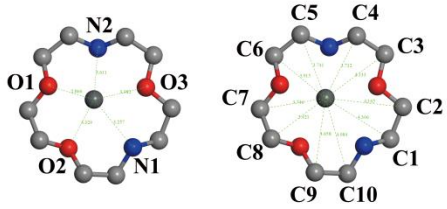

atom	Distance (Å)	atom	Distance (Å)	atom	Distance (Å)
O1	2.866	C1	4.306	C6	3.915
O2	3.329	C2	4.165	C7	3.746
O3	3.382	C3	4.133	C8	3.421
N1	3.257	C4	3.712	C9	3.658
N2	3.611	C5	3.741	C10	4.084

Figure S6. The distances between carbon, oxygen and nitrogen atoms and lead atom in DFT analysis. Atoms are numbered outside the ring. Hydrogen and iodide atoms are hidden for easy observation. The gray, red, blue and black colors indicate C, O, N and Pb atoms respectively.

Note S1. *Calculation of distances between CEs and Pb^{2+}*

In order to distinguish the interaction distance between Pb^{2+} and CEs, firstly we show the distances between carbon, oxygen and nitrogen atoms and lead atom in **Figure S6**. Then we calculate the average distances in **Table S3**. Interestingly, [Pb-all] distances of 15-membered crown ethers (i.e., A15C5 and DA15C5) are closer than those of 18-membered crown ethers (i.e., A18C6 and DA18C6), which mainly results from smaller cavity sizes of 15-membered crown ethers, instead of stronger interaction with Pb^{2+}.

Furthermore, we consider that the vertical distance between Pb and CE plane is more accurate to compare the interaction distance (**Figure S7**). Most of the atoms in CEs (i.e., C, N and O) are non-coplanar, so we determine the plane approximately by mathematical methods as follows. We record C, N and O atoms in the ring as Point α_1, α_2, ... , α_n (n=15 or 18) and the vertical distance from α_n to the plane as d_n. Next, we denote the square sum of d_n as P_{sum} (P_{sum} >0). Then we determine the plane equation in 3D coordinates, which satisfies the minimum value of P_{sum}. In other words, the plane is determined for evenly distributing C, N and O atoms on and below the plane. Lastly, Pb-CE plane distances are calculated in **Table S4**. The Pb-CE plane distances from big to small are A15C5, DA15C5, A15C5, A18C6, DA18C6, 18C6, which are consistent with the side views in **Figure S5**.

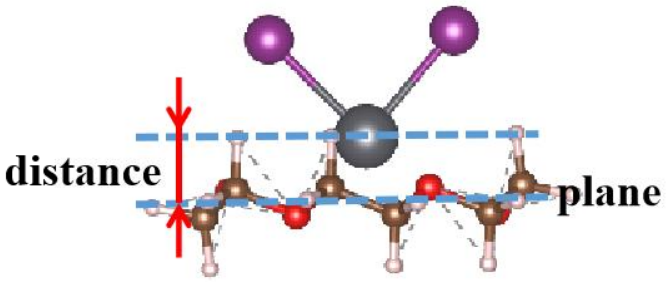

Figure S7. Schematic diagram of the calculation of Pb-CE plane distances.

Note S2. *Experimental methods for ultraviolet-visible titration*

PbI_2, FAI and CEs are dissolved in anhydrous DMF to prepare the below solutions, respectively (denoted as solution ①-⑨ in **Table S5**). For the forward experiment (**Figure 2a-f**), solution⑦ is quantitatively added into solutions ①-⑥, respectively. The volume of FAI solution is used to calculate the ratio of FAI and PbI_2. The reactions can be described as Equation 1-2 for PbI_2 solution and Equation 3-4 for PbI_2-CE mixed solution in **Note S3**. CL is the shorthand for crown ether ligand (e.g., A18C6, 18C6) in the equation. It should be noted that PbI_5^{3-} and PbI_6^{4-} are hardly observed in solution because of their intentionally low concentrations.

For the reverse experiment (**Figure 2h-i**), solution⑨ is quantitatively added into solution⑧, which is described as Equation 5-6. The prepared solutions are placed in quartz cuvettes for recording photos and UV-vis tests.

Note S3. *Chemical reactions for ultraviolet-visible titration*

For forward titration,

$$PbI_2 + I^- \rightleftharpoons PbI_3^- \quad \text{(Equation 1)}$$

$$PbI_3^- + I^- \rightleftharpoons PbI_4^{2-} \quad \text{(Equation 2)}$$

$$PbI_2(CL) + I^- \rightleftharpoons PbI_3(CL)^- \quad \text{(Equation 3)}$$

$$PbI_3(CL)^- + I^- \rightleftharpoons PbI_4(CL)^{2-} \quad \text{(Equation 4)}$$

For reverse titration,

$$PbI_4^{2-} + (CL) \rightleftharpoons PbI_3(CL)^- + I^- \quad \text{(Equation 5)}$$

$$PbI_3^- + (CL) \rightleftharpoons PbI_2(CL) + I^- \quad \text{(Equation 6)}$$

Note S4. *DLS analysis of iodoplumbates*

According to the literature[14-16], the colloidal sizes are directly correlated with the colloid composition. With adding excess I^-, iodoplumbates are split into smaller colloids due to the formation of iodide-rich iodoplumbates. In other words, reduced colloidal particle sizes are observed owing to the further iodation of iodoplumbates[15].

We conducted DLS measurements of the mixture of 0.001 mol/L PbI_2 and 0.1 mol/L FAI in DMF. In the absence of A18C6, by mixing FAI and PbI_2 with the molar ratio of 100:1, we monitor the colloidal sizes of 23 nm and 213 nm (**Figure S8**). Moreover, when mixing A18C6, PbI_2 and FAI at the molar ratio of 1:1:100, increased colloidal sizes of 43 nm and 437 nm are observed. From the inside optical photo, the solutions without and with A18C6 show dark yellowish green and nearly colorless respectively, confirming the different concentrations of iodoplumbates, in agreement with ultraviolet-visible titration.

In solution without A18C6, the small colloidal sizes indicate that iodide-rich iodoplumbates such as massive PbI_3^- and PbI_4^{2-} are formed, which yield smaller perovskite crystals in the films after annealing[17]. Less halogen sharing among $[PbI_6]$ octahedra will separate coordination units and induce a smaller colloidal framework or even individual octahedral units. Correspondingly, increased colloidal sizes in solution with A18C6 represent the suppressed iodation of iodoplumbates.

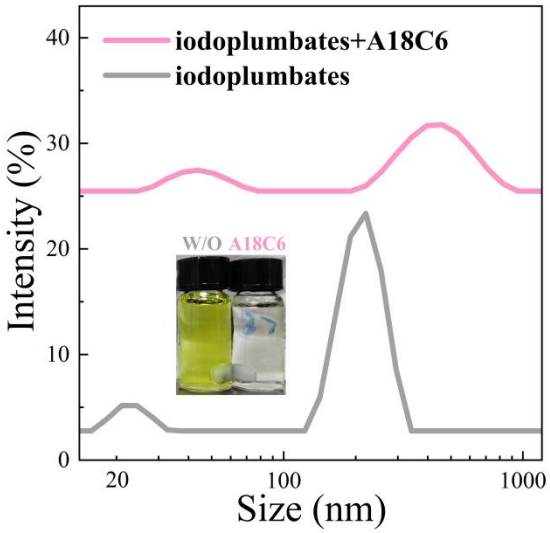

Figure S8. The DLS colloid size distributions in the iodoplumbates solution.

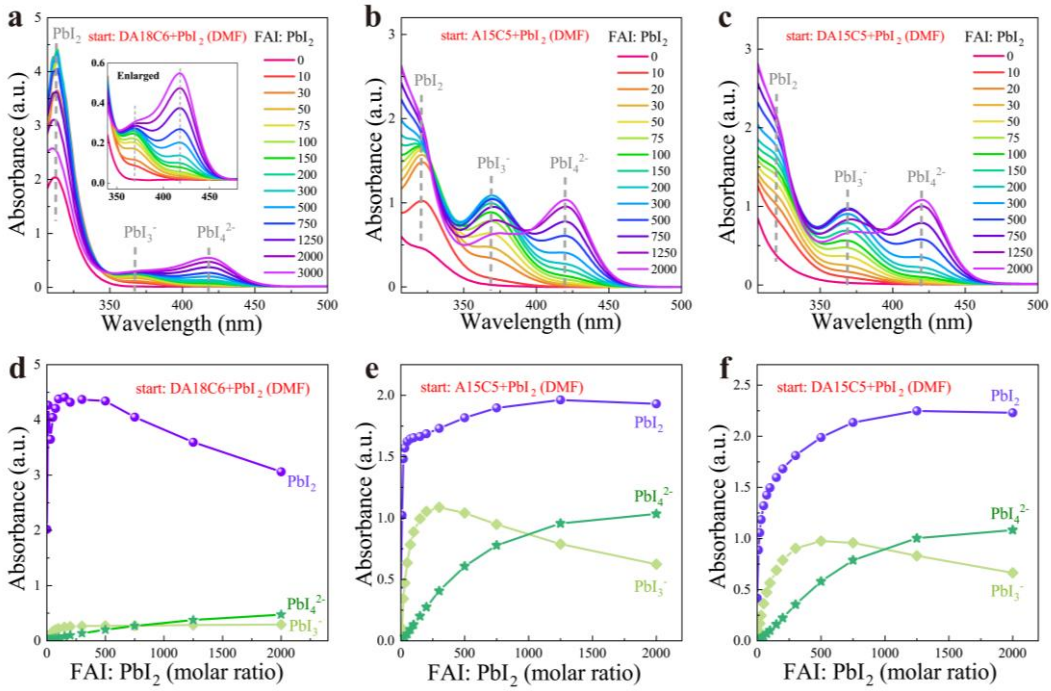

Figure S9. Absorbance of ultraviolet-visible titration for the forward experiment. (a-c) Absorbance spectra of ACE-doped PbI_2 solution in DMF with increasing concentration of FAI. (d-f) Peak absorbance of PbI_2, PbI_3^- and PbI_4^{2-} as a function of [FAI]:[PbI_2]. The iodoplumbate species are marked in different colors.

Note S5. *Benesi-Hildebrand (BH) analysis*

We conducted Benesi-Hildebrand (BH) analyses[18,19] in Equation 7 for PbI_2 solution and Equation 8 for PbI_2-CE mixed solution. CL is short for crown ether ligand in the equation. The general equation of reaction and corresponding formation constant are shown in Equation 9-10, where ligand, M and ligand·M_n are abbreviations of PbI_3^-, I^- and PbI_4^{2-}, and K_f is the formation constant. Combined with Lambert-Beer Law, the BH equation is given in Equation 11-12. A_0 is the initial absorbance of ligand·M_n, A is the absorbance of ligand·M_n during titration, A_{max} is the absorbance of ligand·M_n in the presence of maximum amount of I^-, and [M] is the concentration of I^-. Here, we assume a 1:1 association (i.e., n=1) between CL and iodoplumbates[20].

$$PbI_3^- + I^- \rightleftharpoons PbI_4^{2-} \quad \text{(Equation 7)}$$

$$PbI_3(CL)^- + I^- \rightleftharpoons PbI_4(CL)^{2-} \quad \text{(Equation 8)}$$

$$\text{ligand} + n\text{M} \rightleftharpoons \text{ligand}\cdot\text{M}_n \quad \text{(Equation 9)}$$

$$K_f = \frac{[\text{ligand}\cdot\text{M}_n]}{[\text{ligand}]\cdot[\text{M}]^n} \quad \text{(Equation 10)}$$

$$\frac{1}{A - A_0} = \frac{1}{K_f(A_{max}-A_0)[\text{M}]^n} + \frac{1}{A_{max} - A_0} \quad \text{(Equation 11)}$$

$$\lg\frac{A-A_0}{A_{max} - A} = n\lg[\text{M}] + \lg K_f \quad \text{(Equation 12)}$$

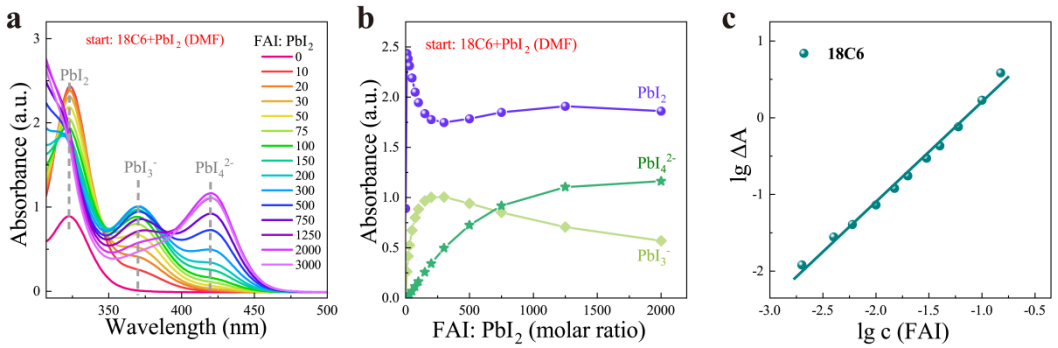

316

317 **Figure S10.** Absorbance of ultraviolet-visible titration for 18C6-doped PbI_2. (a)
318 Absorbance spectra of 18C6-doped PbI_2 solution in DMF with increasing concentration
319 of FAI. (b) Peak absorbance of PbI_2, PbI_3^- and PbI_4^{2-} as a function of [FAI]:[PbI_2]. (c)
320 The linear fitting of BH analysis.

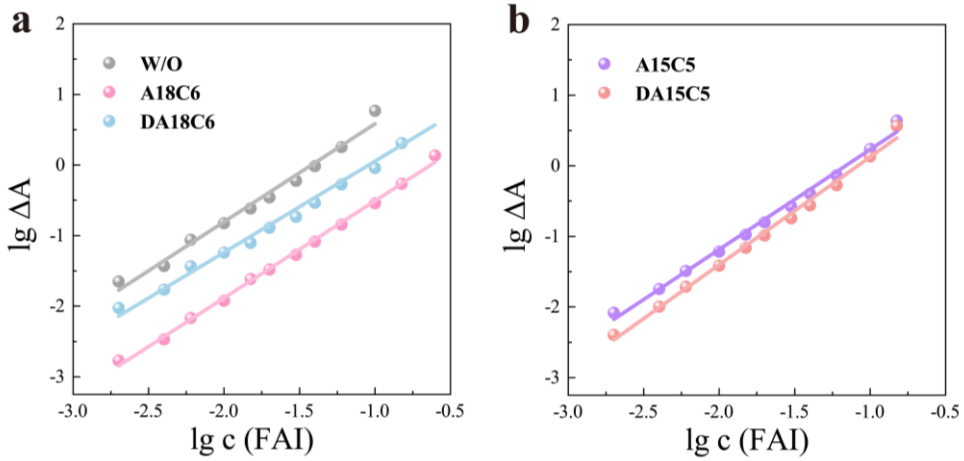

Figure S11. The linear fitting of BH analysis.

ΔA is short for $(A\text{-}A_0)/(A_{max}\text{-}A)$ and c (FAI) is the concentration of I^-. The formation constants of PbI_4^{2-} and $PbI_4(CL)^{2-}$ are calculated in **Table S6**.

Note S6. *The side reactions in the precursor solution*

According to the literature[14-16], the perovskite precursor solution is a colloidal mixture of lead polyhalide species (e.g., iodoplumbates) which act as nucleation sites during the crystallization process. It is confirmed that precursor solution suffers from degeneration during different aging conditions and produces detrimental impurities. Therefore, developing scalable and stable precursors and extending the perovskite ink shelf life are vital to batch-to-batch reproducibility.

The chemical reaction equations including Step A-D in **Figure S12** elucidate the aging mechanism in precursor solution. Here, organometal-halide perovskites (OHPs) are simplified as (FA, MA)PbI_3. After mixing FAI/MAI and PbI_2, iodoplumbates form in solution. With increasing the shelf time, formamidinium iodide (FAI) and methylammonium iodide (MAI) undergo deprotonation and produce HI (Step A)[21,22]. In Step B, self-condensation of FAI occurs to form the by-product s, i.e., triazine. MA can react with FAI to form N-methylformamidinium iodide (MFAI), and MFAI further reacts with MA to form N,N'-dimethylformamidinium iodide (DMFAI)[23]. In Step C, the degradation of DMF results in the formation of formic acid (HCOOH) and dimethylamine (DMA), and HI catalyzes the degradation[24].

In Step D, under illumination or oxygen, HI transforms to I_2. I_2 is easy to combine with I^- and creates tri-iodide ion I_3^-. Under visible light/UV, I_2 produces atomic iodine (I•), which binds with I^- bind and generates $I_2^{\bullet-}$. FA^+ cation reacts with $I_2^{\bullet-}$ and forms I_2[25]. These cycle reactions accelerate the formation of I_2.

During the thermal annealing process (Step E), pure α-$FAPbI_3$ films can be obtained by using fresh precursor solution due to the absence of HI. When preparing films by aged solution, δ-$FAPbI_3$ is formed. Because HI disturbs the formation of photoactive α-$FAPbI_3$ and a high concentration of HI favors non-photoactive δ-$FAPbI_3$[21].

Furthermore, we choose the system of $Cs_{0.04}(FA_{0.97}MA_{0.03})_{0.96}Pb(I_{0.97}Br_{0.03})_3$ in this work. The degradation processes of Step A, D and E are mainly considered for the reasons below. Firstly, MAI content is far less than FAI, so the MA-FA^+ reaction in Step B can be neglected. It is also reported that Cs^+ significantly slows down the MA-FA^+ reaction[26]. Besides, the hydrolysis of DMF (Step C) proceeds slowly at room temperature, and the usage of anhydrous DMF also decelerates the process[24].

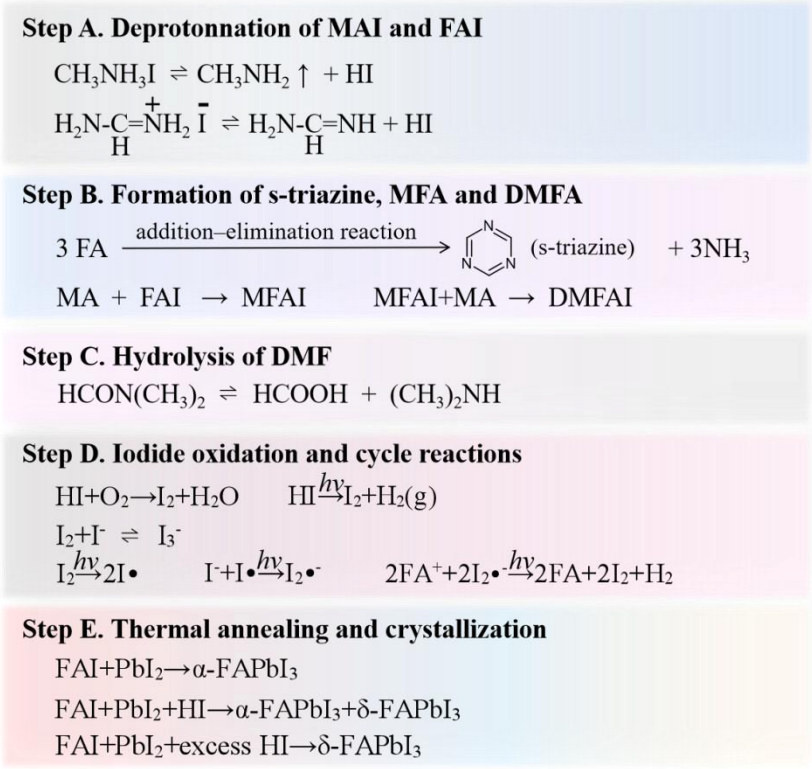

358

359 **Figure S12.** Degradation mechanisms of perovskite precursor solution.

Note S7. *The characterizations of perovskite films fabricated by N_2-aged precursor solutions*

In this experiment, we prepare perovskite precursor with the composition of $Cs_{0.04}(FA_{0.97}MA_{0.03})_{0.96}Pb(I_{0.97}Br_{0.03})_3$. The sealed perovskite precursor solutions without and with A18C6 are aged in N_2 glove box in dark for 0 and 120 days, respectively. 0.4 mmol/L A18C6 is added to the precursor solution.

As shown in **Figure S14a**, the perovskite films without and with A18C6 prepared by fresh solutions show an absorption edge of 800 nm. The sample prepared by aged solution with A18C6 exhibits a slight decrease in the wavelength of 550-650 nm and basically no change around 800 nm, while that without A18C6 presents significantly reduced light absorption from 550 nm to 800 nm. In addition, the perovskite film prepared with aged precursor solution with A18C6 shows a higher ratio of α-$FAPbI_3$ / δ-$FAPbI_3$ in **Figure S14b**. Moreover, The average TRPL lifetime of perovskite films without and with A18C6 decays over the aging time of precursor, while the perovskite film with A18C6 shows less lifetime attenuation (**Figure S14c, Table S8**). This originates from the stabilization of iodoplumbates and the remarkably retarded production of HI and I_2 (i.e., I_3^-) by A18C6.

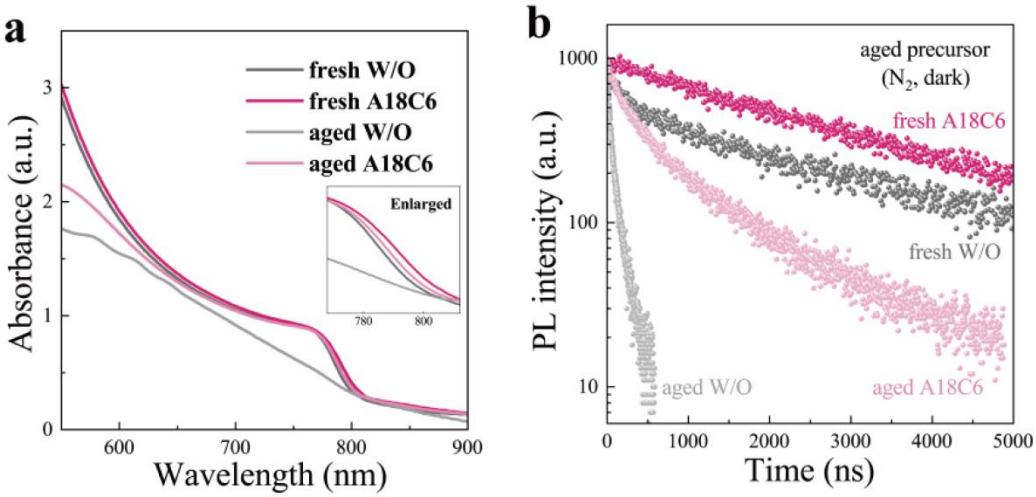

Figure S13. Film characterizations prepared by fresh and aged solutions. The perovskite precursor solutions are aged in N_2 glove box for 0 and 120 days. (a) UV-vis absorbance of the perovskite films. (b) TRPL decays of the perovskite films.

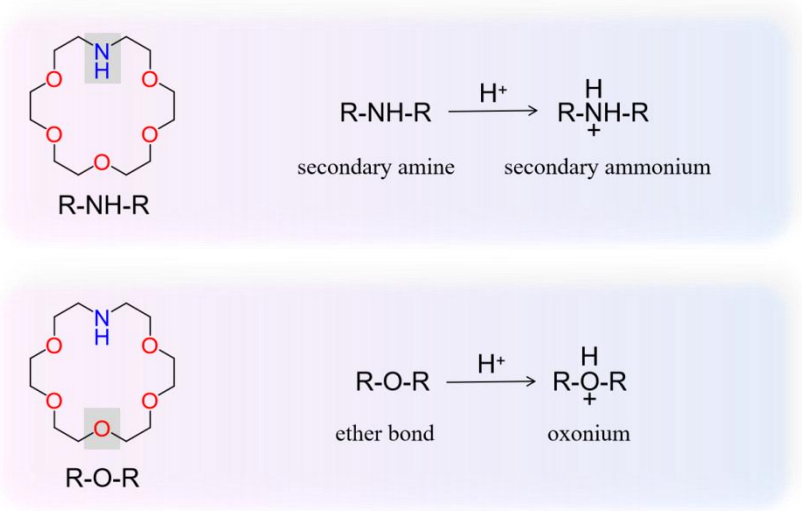

Figure S14. Lewis base functional groups and their reactions with hydrogen ion.

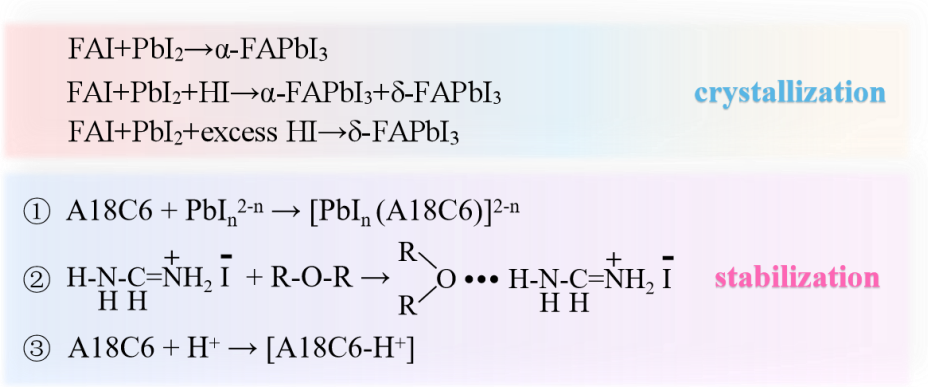

Figure S15. Stabilization mechanisms of perovskite precursor solution involved by A18C6.

Note S8. *The stabilization mechanism by A18C6*

In consideration of the chemical properties of A18C6, the ether bonds and the secondary amine are the main functional groups (**Figure S14**). The stabilization mechanisms of perovskite precursor solution involved by A18C6 contain three parts (**Figure S15**). Firstly, A18C6 binds with iodoplumbates and stabilizes the colloids. Secondly, the O atom in A18C6 forms hydrogen bond with the H atom in FA^+ cation, inhabiting the degradation of FAI. Thirdly, the electronegative O and N atoms in A18C6 bind with H^+ via lone pair electrons and produce oxonium and secondary ammonium, which prevent HI to accelerate the formation of δ-$FAPbI_3$.

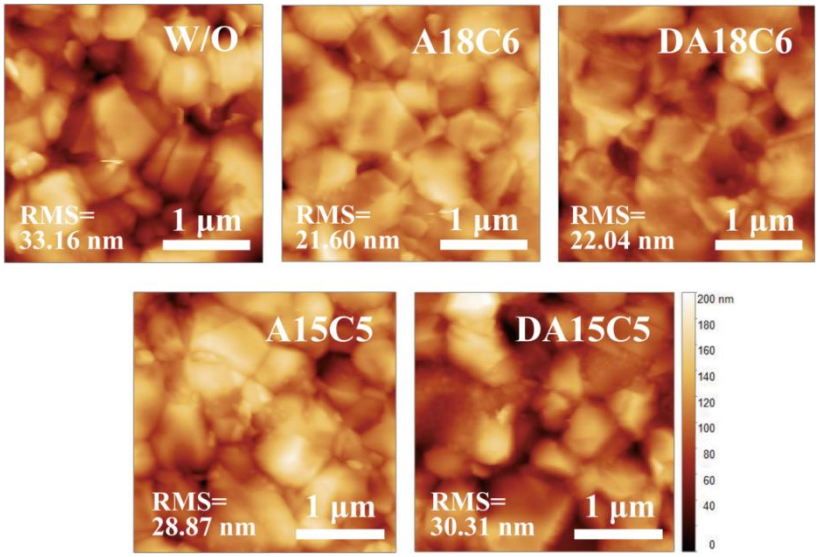

Figure S16. AFM topography of perovskite films. Root mean square roughness (RMS) is indicated inside the figure.

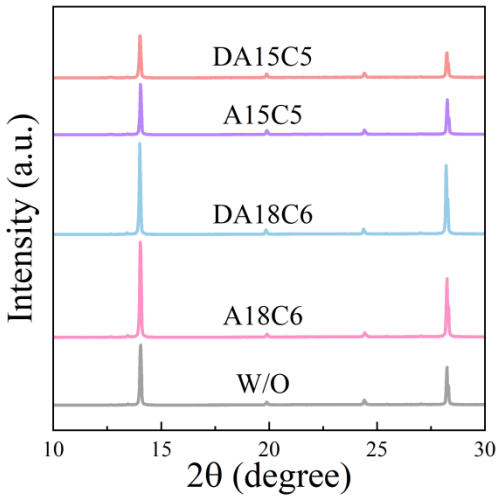

Figure S17. XRD patterns of perovskite films, W/O and with ACE modification, respectively.

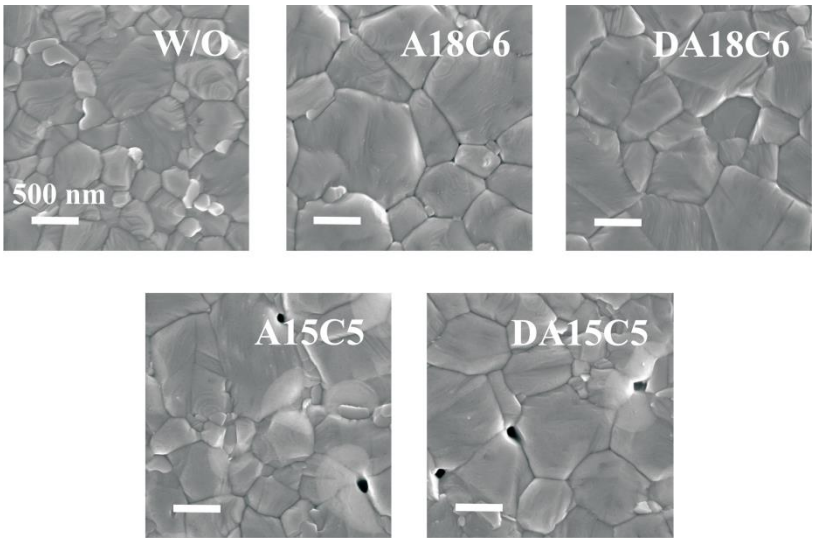

Figure S18. Surface SEM images of the perovskite films without and with ACEs modification under high magnification.

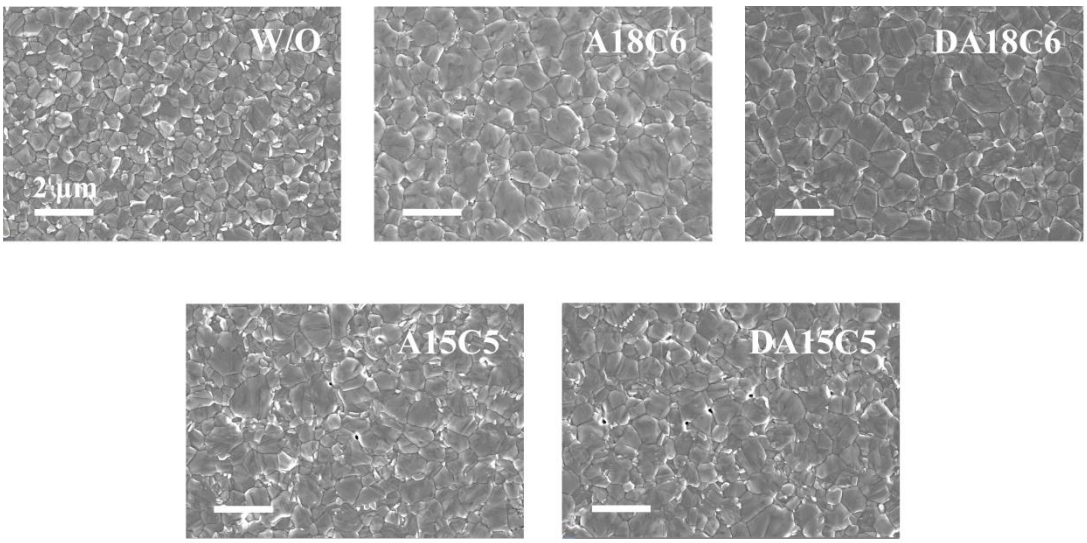

Figure S19. Surface SEM images of the perovskite films, without and with ACEs modification under low magnification.

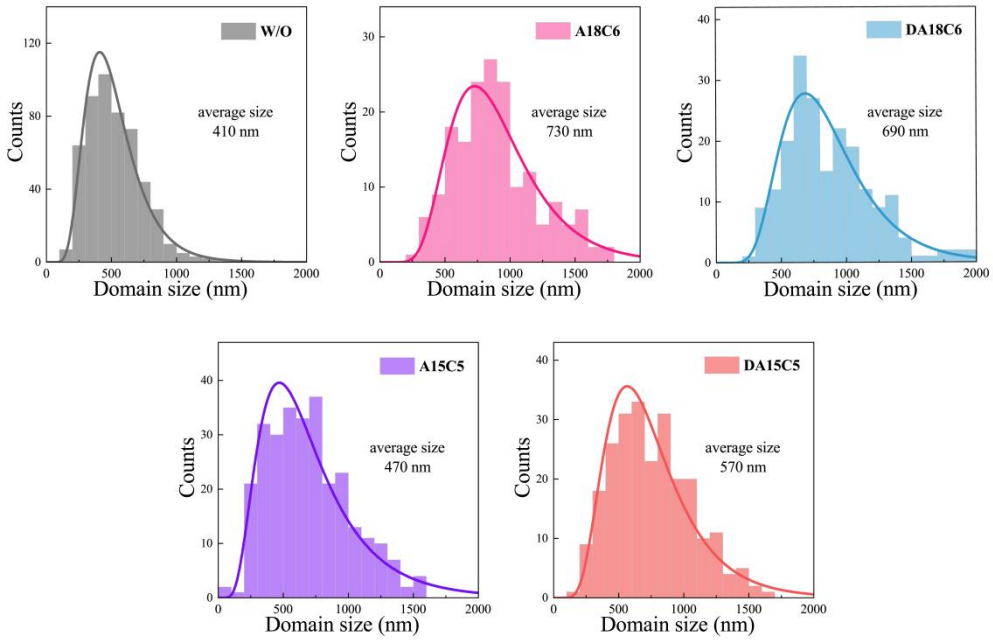

407

408 **Figure S20.** Statistical graphs of average domain size derived from low magnification
409 SEM images of perovskite films.

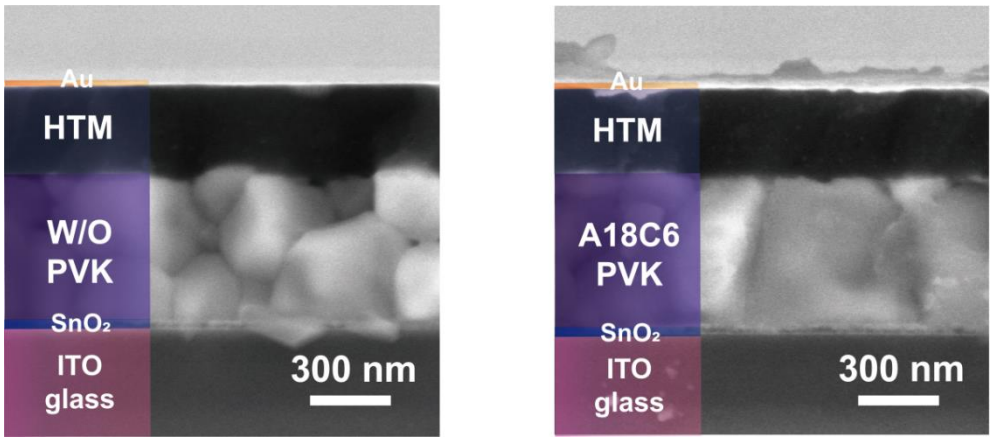

Figure S21. Cross-section SEM images of devices without and with A18C6 modification.

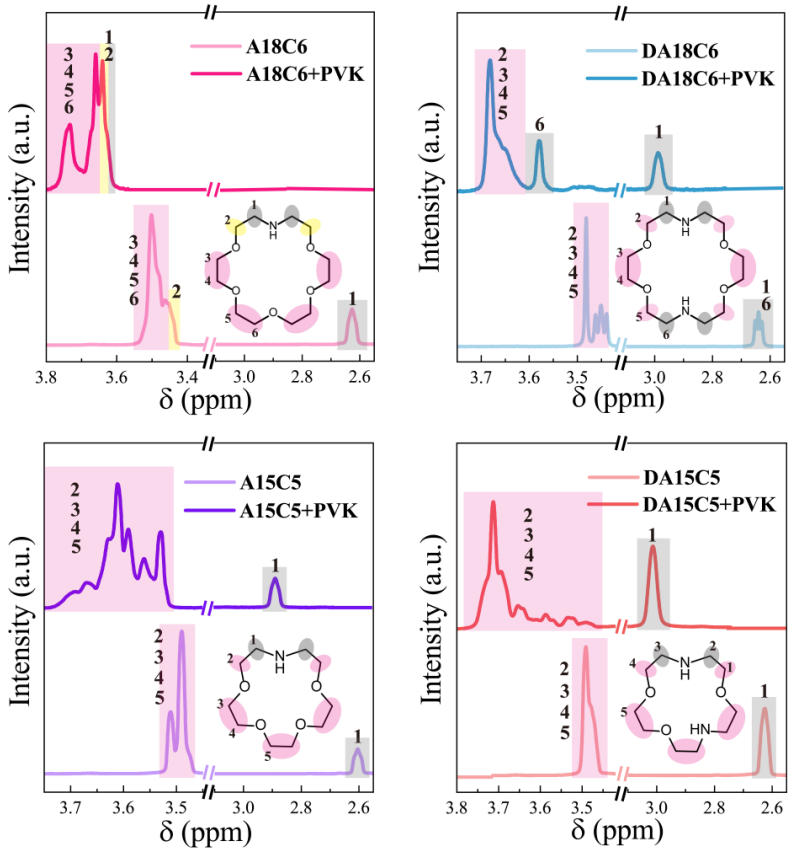

Figure S22. Enlarged ^{1}H-NMR liquid-state spectra of ACE solutions and ACE-PVK solutions. The hydrogen atoms on different carbon atoms are marked in different colors.

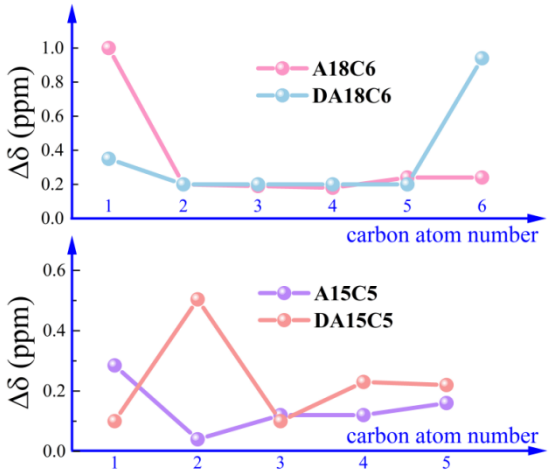

Figure S23. Chemical shift change ($\Delta\delta$) between ACE-PVK and ACE, calculated by the following formula: $\Delta\delta = \delta$ (ACE-PVK) - δ (ACE). The positions of H atoms are distinguished by integrated peak areas in NMR spectra. The average chemical change ($\Delta\delta_{ave}$) values of A18C6, DA18C6, A15C5 and DA15C5 are 0.342, 0.348, 0.145 and 0.231, respectively.

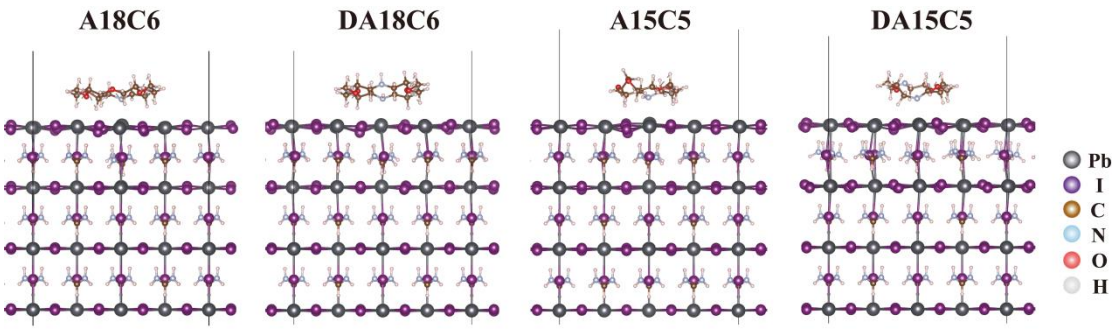

Figure S24. The DFT-optimized atomic structure of ACEs binding on the perovskite surface.

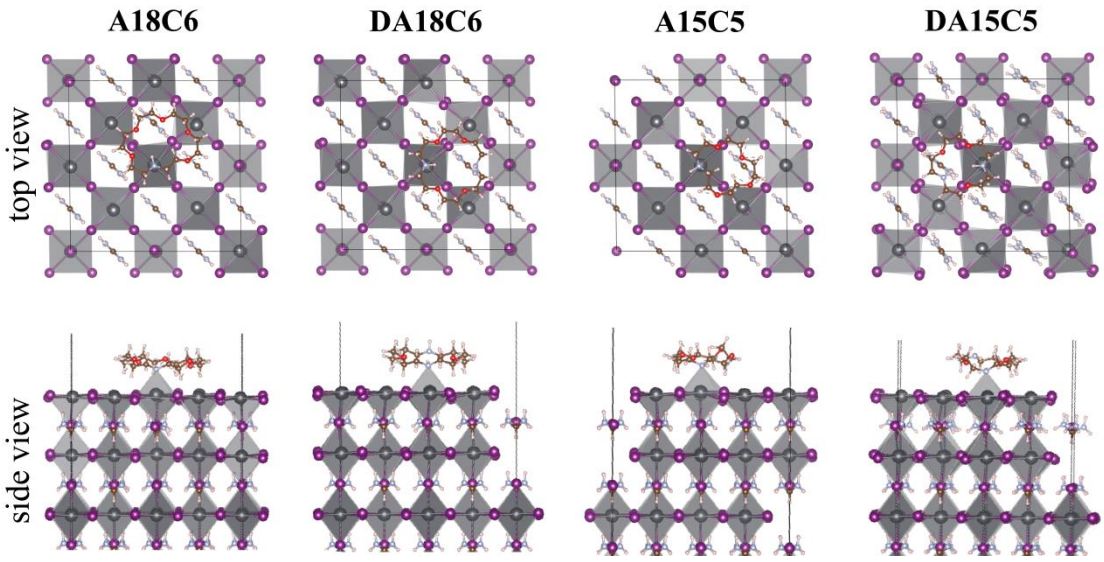

425

426 **Figure S25.** Top and side views of the DFT-optimized atomic structure of ACEs
427 binding on the perovskite surface. The brown, white, red, ice-blue, gray and purple
428 colors indicate C, H, O, N, Pb and I atoms respectively.

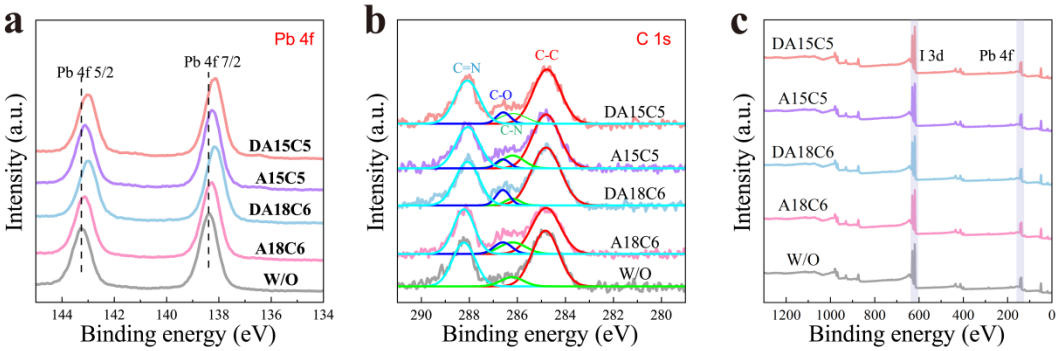

Figure S26. High-resolution XPS spectra of (a) Pb 4f, (b) C 1s and (c) full spectra of perovskite films.

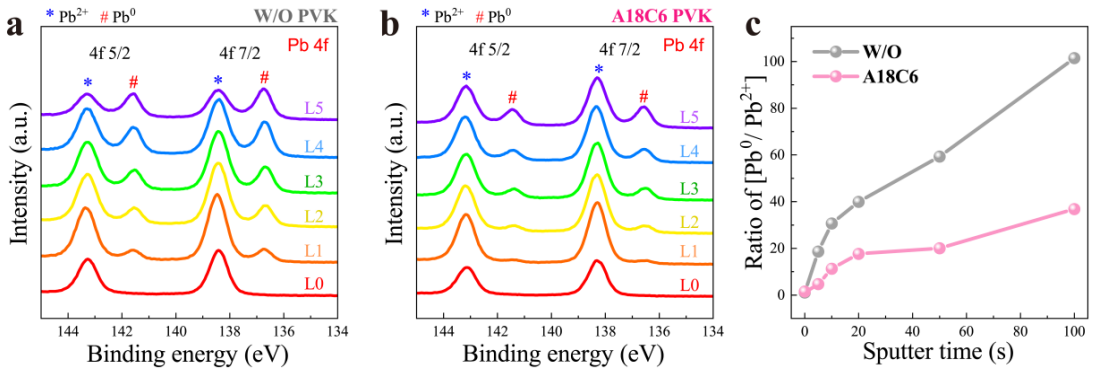

Figure S27. XPS depth profiles of perovskite films. (a, b) Pb 4f of (a) W/O and (b) with A18C6. L0 is the surface layer without ion beam etching. (c) The ratio (%) of Pb^0 and Pb^{2+} with the variation of depth.

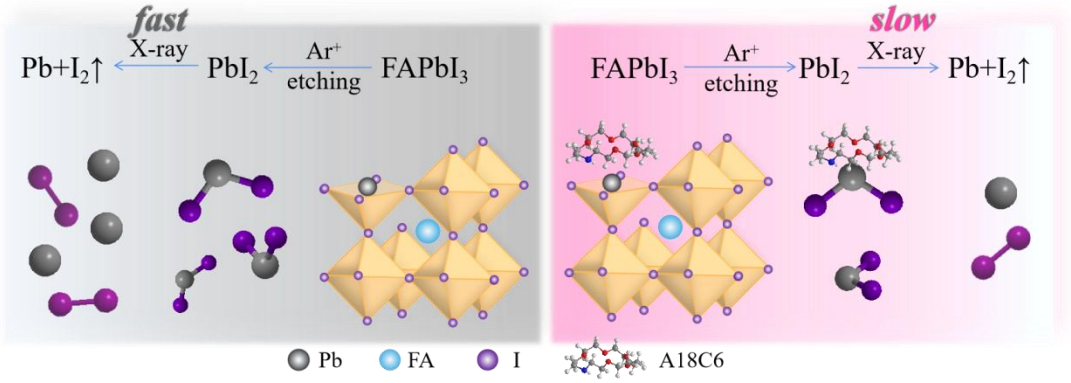

436

437 **Figure S28.** The schematic diagram showing the degradation of $FAPbI_3$ to PbI_2 and Pb.

Note S9. *Commentary of depth-resolved XPS*

We carried out depth-resolved XPS analysis of perovskite films without and with A18C6, and calculated the ratio of Pb^0 and Pb^{2+} (%) with the variation of depth (**Figure S27**). The XPS spectra of Pb 4f level range exhibit two main peaks of Pb $4f_{5/2}$ and Pb $4f_{7/2}$ derived from Pb^{2+}, along with two weak peaks which attribute to metallic Pb. The ratios of [Pb^0/Pb^{2+}] gradually increase in perovskite films without and with A18C6 as the depth increases, suggesting the degradation of PbI_2[16]. However, the perovskite film with A18C6 shows less degradation, which probably suppresses the deterioration of performance and operational stability of PSCs. As shown in **Figure S28**, A18C6 inhibits the decomposition of PbI_2 and the production of Pb. We propose that the stabilization effect results from the A18C6-PbI_2 coordination interaction.

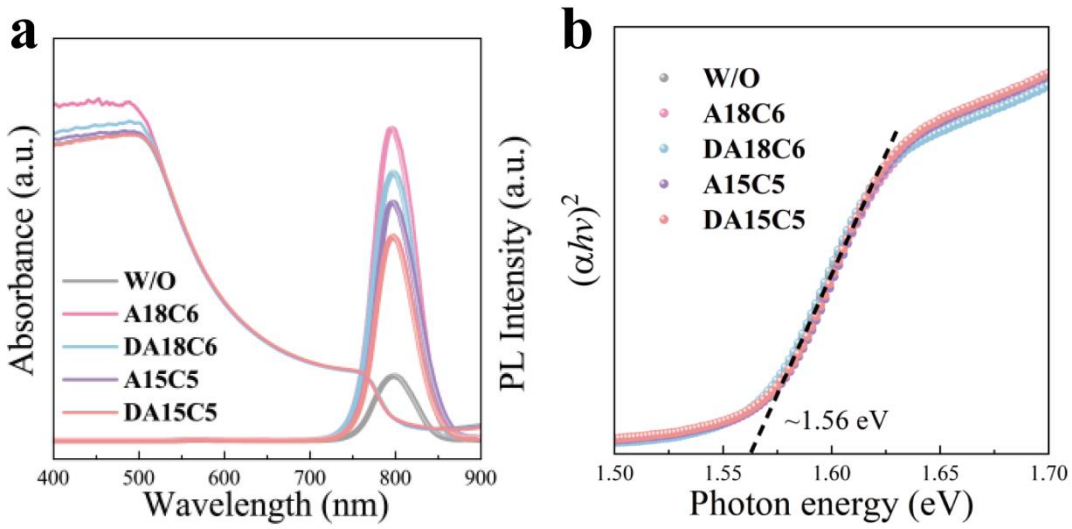

Figure S29. (a) UV-vis absorption and steady-state photoluminescence spectra of the perovskite films. (b) Optical band-gap calculations of perovskite films, without and with ACEs modification, based on UV-vis absorption spectra by using Tauc-plot method. The bandgap is ~1.56 eV.

Figure S30. PL mapping of the perovskite films. Data were obtained over an area of 40 μm × 40 μm.

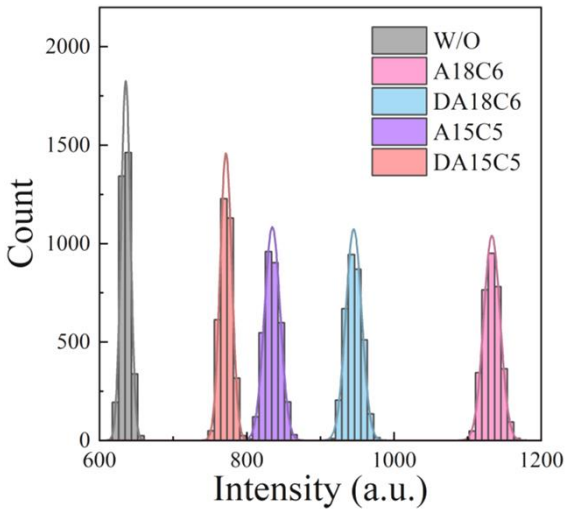

Figure S31. The corresponding statistics diagrams of PL intensity in PL mapping of perovskite films.

Note S10. *Details for Mott-Schottky plots*

We measured Mott-Schottky plots based on Mott-Schottky equation:

$$C^{-2} = 2(V_{bi} - V)/(A^2 e\varepsilon_0\varepsilon_r N_A) \quad \text{(Equation 13)}$$

where V_{bi} is the build-in potential, V is the applied voltage, ε_0 is the vacuum permittivity, ε_r is the relative dielectric constant, e is the electron charge, and N_A is the carrier concentration.

The build-in potential is calculated to study the influence of trap states on charge transport. A higher V_{bi} provides an enhanced driving force for photogenerated carrier separation, resulting in extended depletion region and reduced electron-hole recombination[28].

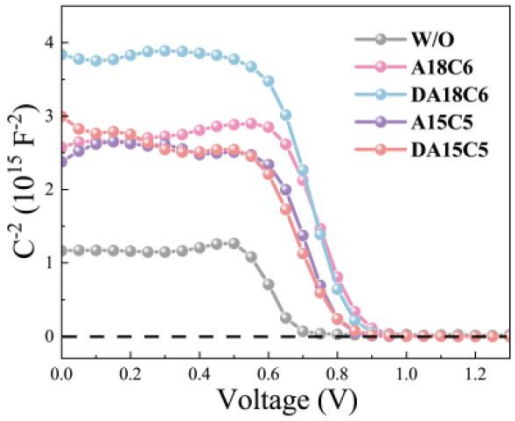

Figure S32. Mott-Schottky plots of PSCs. The V_{bi} values are 0.682 V, 0.807 V, 0.783 V, 0.724 V and 0.693 V for W/O, A18C6, DA18C6, A15C5 and DA15C5 PSCs, respectively.

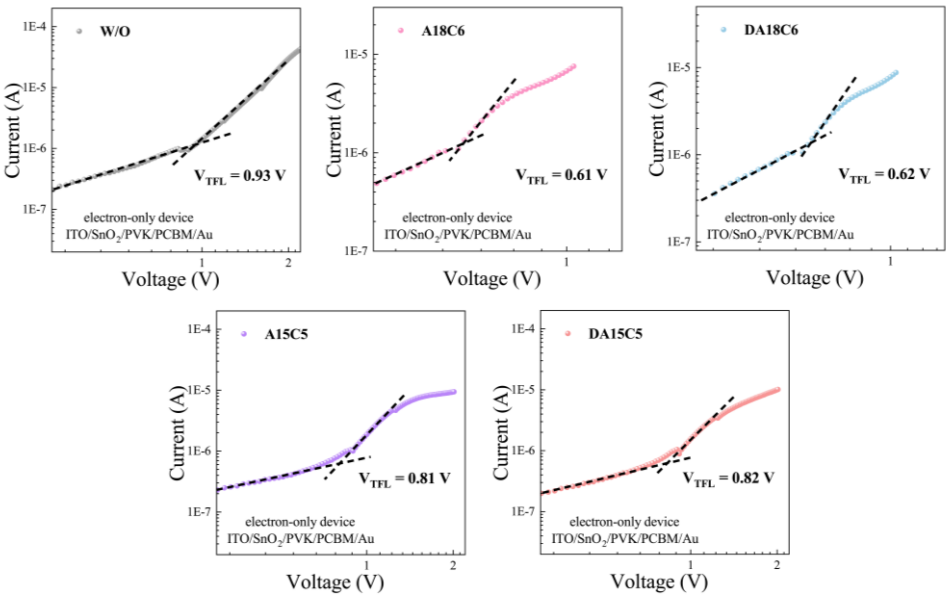

Figure S33. Space-charge limited current characteristics of electron-only devices.

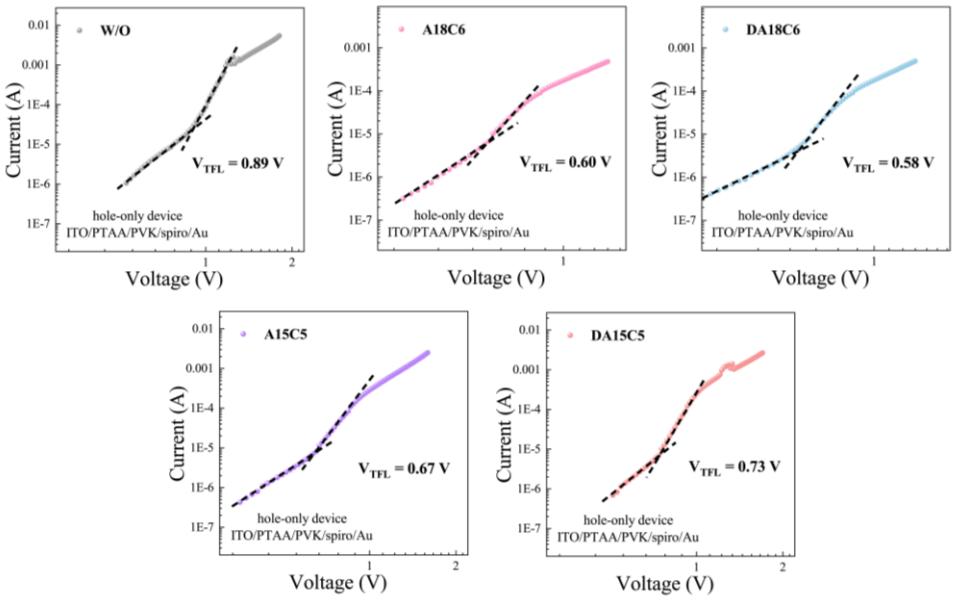

Figure S34. Space-charge limited current characteristics of hole-only devices.

Note S11. *Details for light intensity-dependent V_{oc} measurements*

We studied the light intensity-dependent *J-V* characteristics of PSCs. The relationship between V_{oc} and light intensity (P_{light}) can be expressed by Equation 14

$$V_{oc} = (nkT/q) \ln (P_{light}) \quad \text{(Equation 14)}$$

where n is the ideality factor of the diode which is in the range of 1-2, k, T and q represent the ideality factor, Boltzmann constant, the absolute temperature and the elementary charge, respectively. Usually, a slope higher than 1 kT/q suggests the existence of trap-assisted recombination[29]. A slope close to 1 indicates reduced trap-assisted recombination.

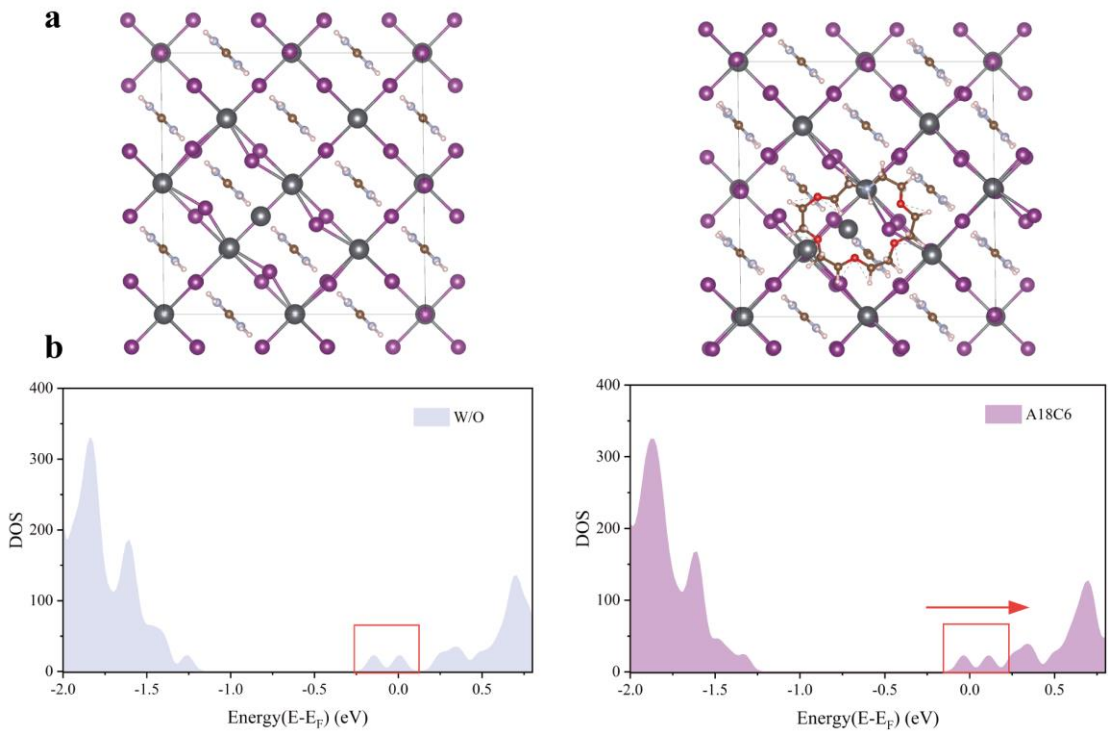

Figure S35. (a) Adsorption structure of the surface Pb_I antisite defect without or with A18C6 treatment. (b) Density of states (DOS) of the surface Pb_I antisite defect without or with A18C6 treatment.

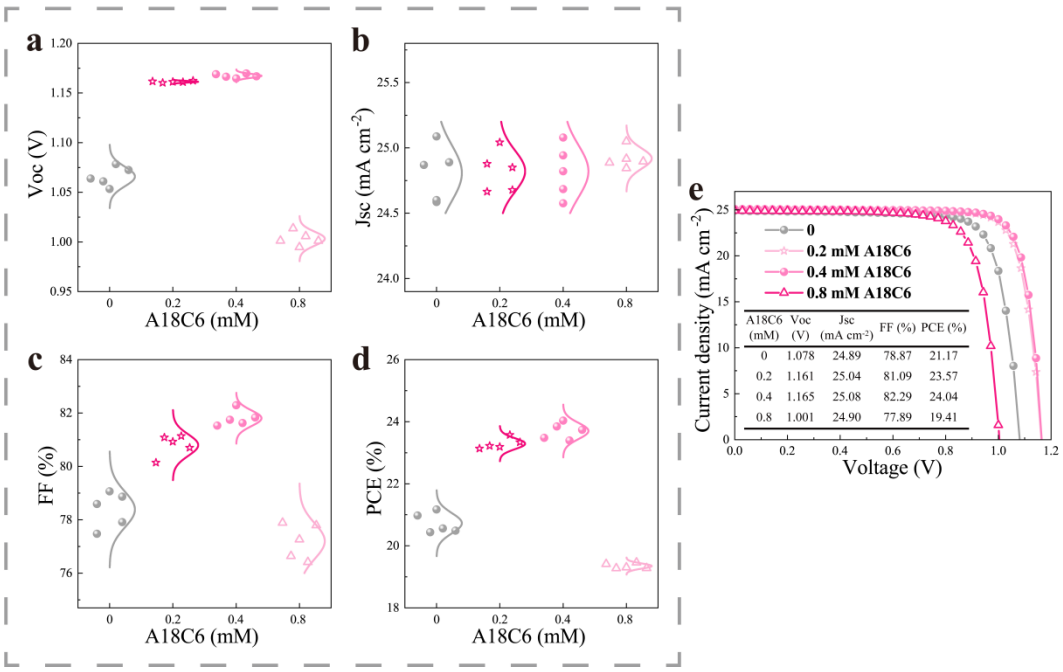

Figure S36. Performance of PSCs without and with A18C6 modification. (a-d) The statistical distribution of (a) V_{oc}, (b) J_{sc}, (c) FF, and (d) PCE. (e) *J-V* characteristics of the champion devices.

Notes:

When 0.2 mmol/L A18C6 is used, the performance of PSCs is improved. When the concentration is increased to 0.4 mmol/L, the devices yield the best PCE. Further increasing the concentration to 0.8 mmol/L results in serious device performance degradation.

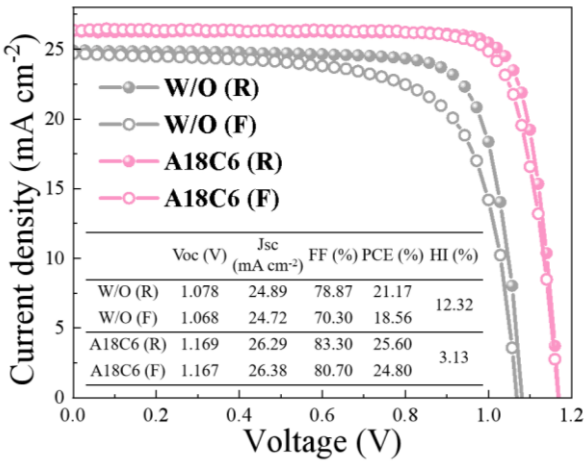

506

507 **Figure S37.** *J-V* characteristics of champion devices under reverse scan (R) and
508 forward scan (F), with an active area of 0.08313 cm^2.

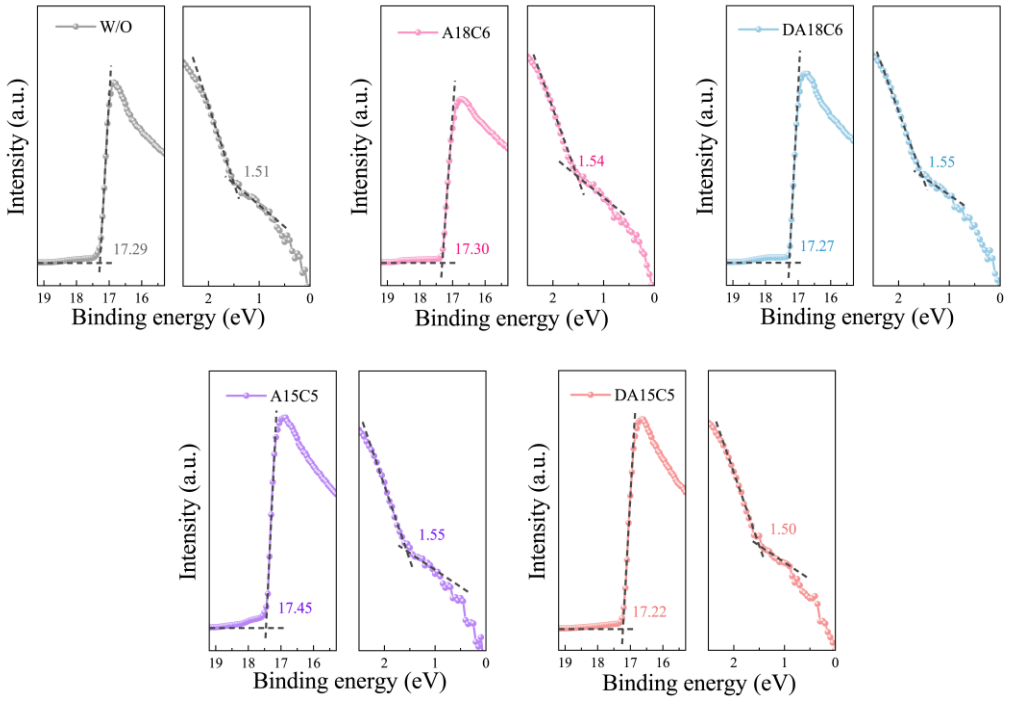

509

510 **Figure S38.** The high-binding-energy and the low-binding-energy cutoffs in UPS
511 spectra of perovskite films, without and with ACEs modification.

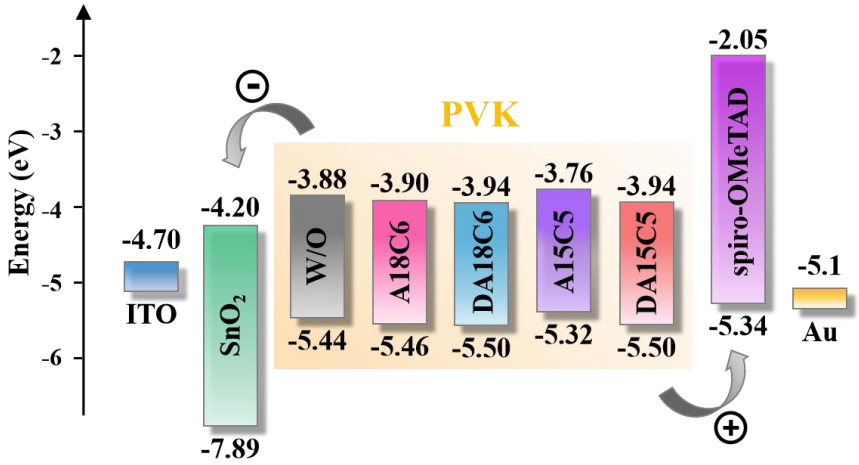

512

513 **Figure S39.** Energy band diagrams of perovskite solar cells based on a structure of
514 ITO/SnO_2/PVK/spiro-OMeTAD/Au.

Note S12. *Details for UPS measurements*

We conducted ultraviolet photoelectron spectroscopy (UPS) to investigate the energy band structure of PSCs with an architecture of ITO/SnO_2/PVK/spiro-OMeTAD/Au. The surface band structures of perovskite layers without and with ACEs show little change due to the trace amount of ACEs (**Figure S38-39**).

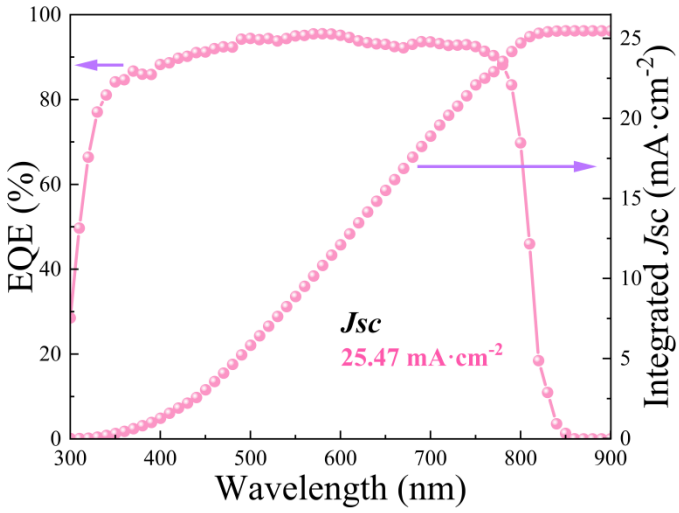

Figure S40. External quantum efficiency (EQE) spectrum of champion device.

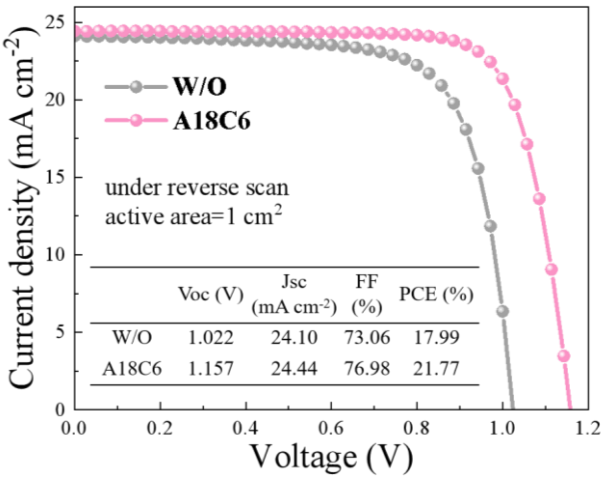

Figure S41. *J-V* characteristics of the champion devices with an active area of 1.0 cm^2.

Note S13. *Synthesis and characterizations of single crystals*

We synthetised $FAPbI_3$ and $MAPbBr_3$ single crystals by inverse temperature crystallization (ITC) method[30], and the details were described in Methods. In **Figure S42a**, in the left picture, the solution is at room temperature. In the right picture, the solution is 150 °C after gradient heating, and some mosaic crystals are grown due to fast heating of solution and high solution concentration. According to literature, big and well-shaped single crystals are often used as X-ray detectors, which can be obtained by low precursor concentration and slow heating of solution[30]. However, single crystals are just used as solutes of perovskite precursors in our work, so the shape and size of crystals are not strictly required. Besides, large crystals are not easy to weigh, so we grind single crystals to powder. Pictures of freshly prepared $FAPbI_3$ crystals are shown in **Figure S42b-c**. The α-$FAPbI_3$ crystals are shiny black with the side-length of 2-6 mm. The cubic phase (α-$FAPbI_3$) suffers from lattice stress and is not stable at room temperature, thus it transforms into yellow phase (δ-$FAPbI_3$) spontaneously even in nitrogen atmosphere. As **Figure S42d** shows, the freshly-prepared $FAPbI_3$ crystals are black, and they experience fast phase transition to δ-$FAPbI_3$. After 24 h storage in nitrogen, almost all the α-$FAPbI_3$ crystals transform to δ-$FAPbI_3$.

In **Figure S42e**, bright orange $MAPbBr_3$ crystals are grown at 100 °C in the third hour of crystallization. The nanocubes are partly inlaid because of fast heating of solution and high solution concentration as the discussion above. Tetragonal $MAPbBr_3$ crystals with the side-length of 3-6 mm are grown, dried and collected (**Figure S42f-h**).

In order to verify the purity of products, we ground single crystals to powder and performed XRD measurements. In **Figure S42i**, we prepared two samples, which are δ-$FAPbI_3$ (yellow line) and α-$FAPbI_3$ (black line), respectively. The powder XRD of δ-$FAPbI_3$ coincides with previous reports. Due to the instability of the black phase, it rapidly transforms into the yellow phase during the XRD measurement in air (RH 50-60%), so the XRD pattern of the α-$FAPbI_3$ sample is actually a mixture of α and δ phases. The characteristic peaks of α-$FAPbI_3$ are marked in the picture. In **Figure S42j**, the XRD pattern of $MAPbBr_3$ matches well with previous literature.

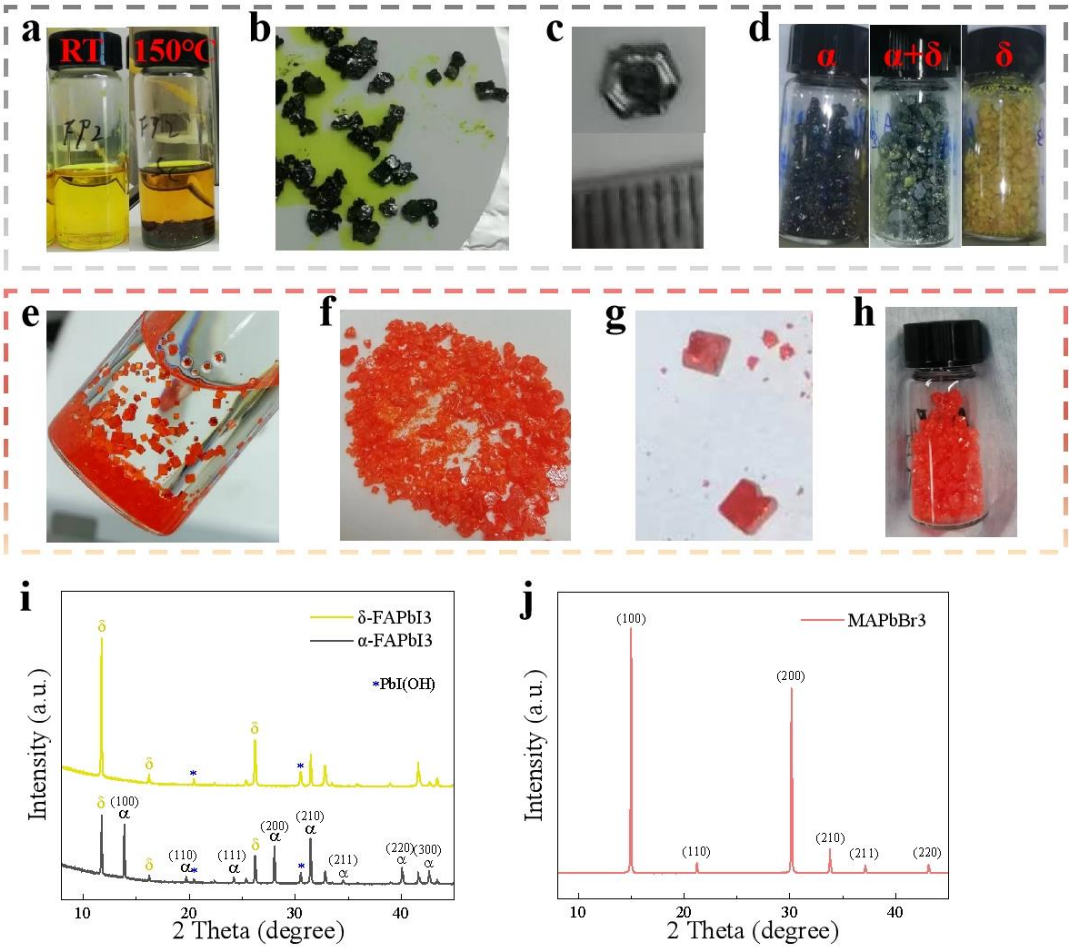

Figure S42. (a) α-$FAPbI_3$ crystal growth at different time intervals. Left, at room temperature (RT), before heating. Right, at 150 °C, the fifth hour. (b,c) Pictures of α-$FAPbI_3$ crystals. (d) The phase transition of α-$FAPbI_3$ to δ-$FAPbI_3$. (e) $MAPbBr_3$ crystal growth at 100 °C, the third hour. (f-h) Pictures of $MAPbBr_3$ crystals. (i) XRD pattern of $FAPbI_3$ powder. (j) XRD pattern of $MAPbBr_3$ powder.

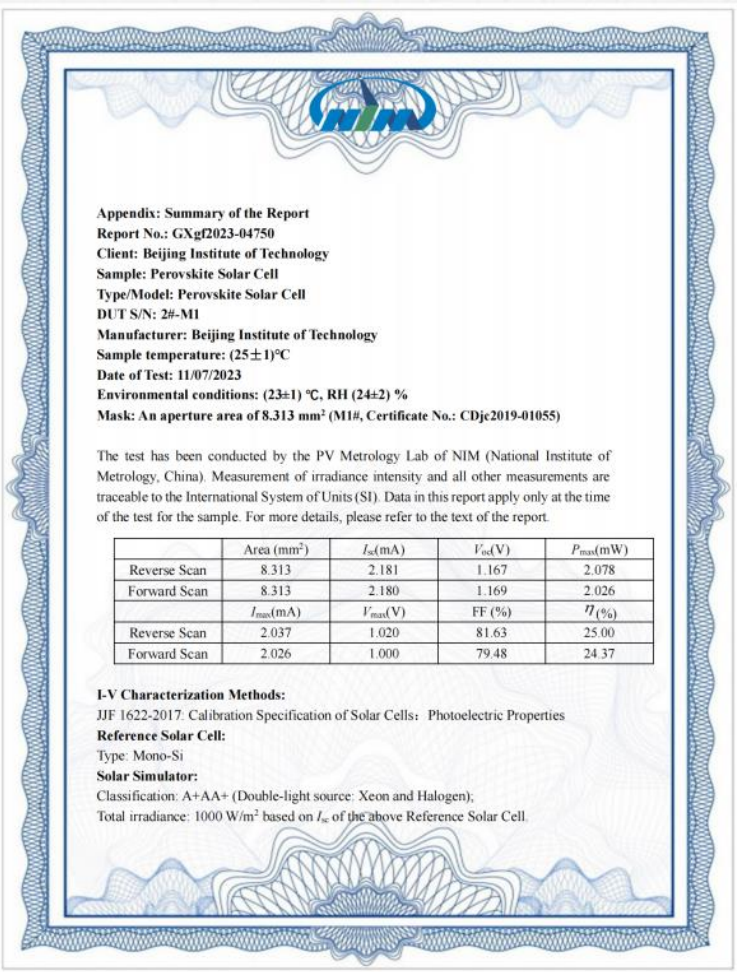

Appendix: Summary of the Report
Report No.: GXgf2023-04750
Client: Beijing Institute of Technology
Sample: Perovskite Solar Cell
Type/Model: Perovskite Solar Cell
DUT S/N: 2#-M1
Manufacturer: Beijing Institute of Technology
Sample temperature: (25±1)℃
Date of Test: 11/07/2023
Environmental conditions: (23±1) ℃, RH (24±2) %
Mask: An aperture area of 8.313 mm² (M1#, Certificate No.: CDjc2019-01055)

The test has been conducted by the PV Metrology Lab of NIM (National Institute of Metrology, China). Measurement of irradiance intensity and all other measurements are traceable to the International System of Units (SI). Data in this report apply only at the time of the test for the sample. For more details, please refer to the text of the report.

	Area (mm^2)	I_{sc}(mA)	V_{oc}(V)	P_{max}(mW)
Reverse Scan	8.313	2.181	1.167	2.078
Forward Scan	8.313	2.180	1.169	2.026
	I_{max}(mA)	V_{max}(V)	FF (%)	η(%)
Reverse Scan	2.037	1.020	81.63	25.00
Forward Scan	2.026	1.000	79.48	24.37

I-V Characterization Methods:
JJF 1622-2017: Calibration Specification of Solar Cells：Photoelectric Properties
Reference Solar Cell:
Type: Mono-Si
Solar Simulator:
Classification: A+AA+ (Double-light source: Xeon and Halogen);
Total irradiance: 1000 W/m² based on I_{sc} of the above Reference Solar Cell.

Figure S43. Certification report of the champion device with crown ether modification by National Institute of Metrology of China (NIM).

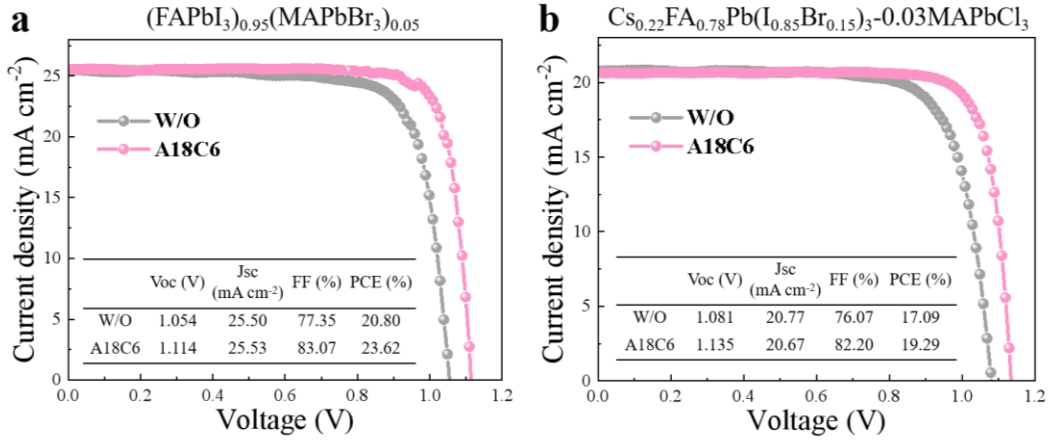

565

566 **Figure S44.** *J-V* characteristics of the champion devices without and with A18C6,
567 containing (a) 1.52 eV [$(FAPbI_3)_{0.95}(MAPbBr_3)_{0.05}$] perovskite and (b) 1.67 eV
568 [$Cs_{0.22}FA_{0.78}Pb(I_{0.85}Br_{0.15})_3-0.03MAPbCl_3$] perovskite. The device structure is
569 ITO/SnO_2/PVK/spiro-OMeTAD/Au.

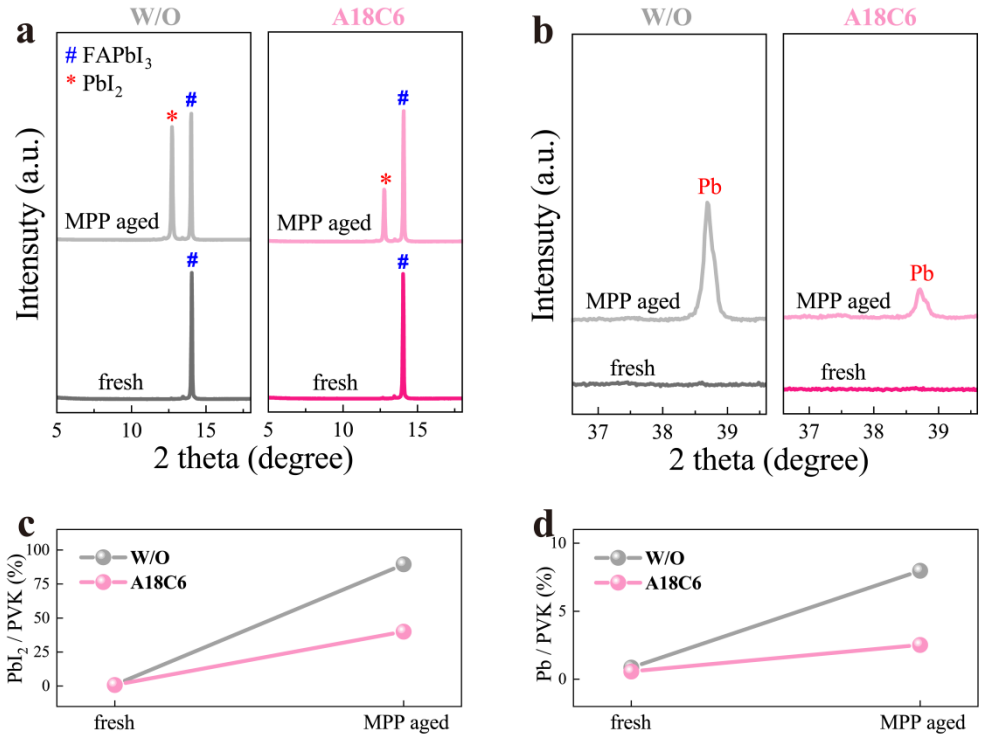

Figure S45. (a,b) Enlarged XRD patterns of the fresh and illumination-aged perovskite films. (c,d) The ratios between PbI_2, Pb and α-$FAPbI_3$ phase.

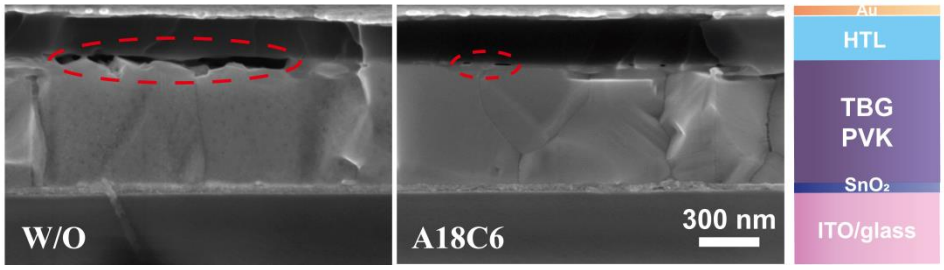

Figure S46. Cross-section SEM images of MPP tracking aged PSCs. Cracks and voids of perovskite were circled with red dotted lines. TBG PVK is short for typical-bandgap perovskite, and HTL is short for hole transport layer.

Note S14. *The decomposition pathways of PSCs*

An overview of decomposition pathways of the illumination-induced PSCs is illustrated by the equations[31]. PSCs starts to decompose and form defects at the structurally vulnerable region (i.e., grain boundaries and PVK/HTL interface). The decomposition generates gas species and PbI_2 (Equation 15). Then PbI_2 degrades to Pb^0 and I_2 (Equation 16). A18C6 passivates the defects at grain boundaries and interfaces, thus effectively suppresses the decomposition of PSCs.

$$FAPbI_3\ (s) \rightarrow PbI_2\ (s) + FA\ (g) + HI\ (g) + HCN\ (g) + NH_3\ (g) \qquad \text{(Equation 15)}$$

$$PbI_2\ (s) \rightarrow Pb\ (s) + I_2\ (g) \qquad \text{(Equation 16)}$$

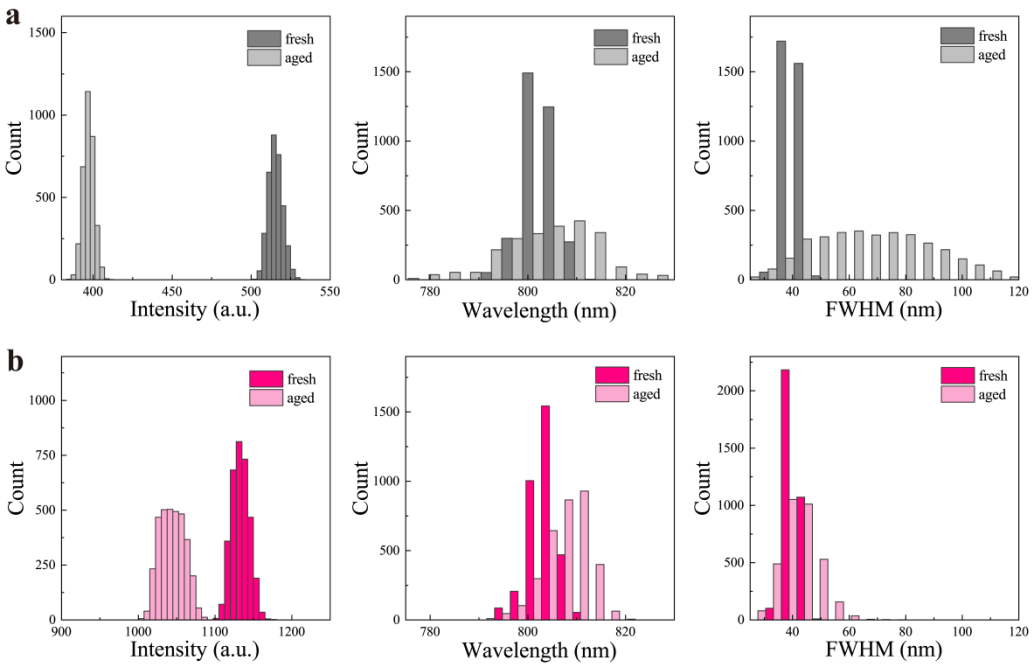

Figure S47. The corresponding statistics diagrams of PL mapping evolution of perovskite films, (a) without and (b) with A18C6.

590 **Table S1**. Summary on crown ether-modified PSCs.

Crown ether	V_{oc} (V)	J_{sc} (mA cm^{-2})	FF (%)	PCE (%)	Operational stability	Reference
12C4	1.14	24.97	81.53	23.24		32
12C4	1.144	23.58	78	21.04		33
15C5	1.16	24.15	76.6	21.5		34
B15C5	1.14	21.1	74.5	18.1		35
18C6	1.06	24.40	79.19	20.48	T_{90} = ~50 h [a)]	36
18C6	1.17	23.63	74.8	20.71		37
18C6	1.17	23.62	74.8	20.71		38
18C6	0.96	22.4	68	14.7		39
DB24C8	1.154	25.80	79.5	23.7	T_{80} = 300 h [b)]	40
DB21C7	1.17	25.50	81.9	24.3	T_{95} = 500 h [b)]	41
DB18C6	1.11	23.84	78.75	20.84	T_{95} = 500 h [c)]	42
A18C6	1.169	26.29	83.30	25.60	T_{95} = 1200 h [b)]	**this work**

591

592 a) under continuous illumination, encapsulated solar module under maximum power point
593 (MPP) measurement at RH 45±5%

594 b) unencapsulated devices under maximum power point tracking, AM 1.5 G, 100 mW/cm^2 in
595 N_2, room temperature.

596 c) unencapsulated devices with AM 1.5 G irradiation at room temperature in N_2.

Table S2. The parameters of different quantum chemical properties of crown ethers.

	Dipole moment (D)	E_{HOMO} (eV)	E_{LUMO} (eV)	Gap (eV)	η (eV)	μ (eV)
18C6	0.0061	-6.600	0.695	7.296	3.648	-2.953
A18C6	0.529	-5.894	1.007	6.901	3.451	-2.443
DA18C6	0.001	-6.005	0.975	6.980	3.490	-2.515
15C5	1.7188	-6.721	1.044	7.765	3.883	-2.839
A15C5	3.543	-6.239	0.771	7.010	3.505	-2.734
DA15C5	0.7831	-5.997	1.003	7.001	3.500	-2.497

Notes:

The energy values of HOMO and LUMO were calculated from density functional theory analysis. Gap, chemical hardness (η) and chemical potential (μ) were derived according to the following formula: $Gap=E_{LUMO}-E_{HOMO}$, $\eta=(E_{LUMO}-E_{HOMO})/2$, $\mu=(E_{LUMO}+E_{HOMO})/2$[43,44].

Table S3. The calculation of average distances in **Figure S7**.

Distance (Å)	Pb-O	Pb-N	Pb-C	Pb-all
A18C6	3.585	3.672	4.082	3.921
DA18C6	3.372	3.274	4.052	3.814
A15C5	3.778	4.128	3.899	3.882
DA15C5	3.192	3.434	3.888	3.688

Notes:

The distance of Pb-all in the last column is calculated by the distances between Pb atom and C, N and O atoms (i.e., the distances between Pb and all the atoms in ACE except H atoms).

609 **Table S4.** The calculation of Pb-CE plane distances in **Figure S6** side view.

610

	Distance of [Pb-CE plane] (Å)
18C6	2.6
A18C6	3.8
DA18C6	2.7
15C5	4.9
A15C5	7.1
DA15C5	5.3

611

612 **Table S5.** Preparation of DMF solutions for ultraviolet-visible titration

solution	solute	
①	0.2 mmol/L PbI_2	
②	0.2 mmol/L PbI_2	0.2 mmol/L A18C6
③	0.2 mmol/L PbI_2	0.2 mmol/L DA18C6
④	0.2 mmol/L PbI_2	0.2 mmol/L A15C5
⑤	0.2 mmol/L PbI_2	0.2 mmol/L DA15C5
⑥	0.2 mmol/L PbI_2	0.2 mmol/L 18C6
⑦	1.5 mol/L FAI	
⑧	0.2 mmol/L PbI_2	0.15 mol/L FAI
⑨	2 mmol/L A18C6	

613

614 **Table S6.** Benesi-Hildebrand analysis of the UV-vis data. The unit of K_f is $(mol/L)^{-1}$.

	intercept	K_f
W/O	1.97	94
A18C6	0.87	7
DA18C6	1.34	22
A15C5	1.65	44
DA15C5	1.65	44
18C6	1.51	32

615

616 **Table S7**. Summary on solution aging and stabilization methods.

Aging conditions	Method	Step	Mechanism	Reference
/	hypophosphorous acid	D	reduce the oxidized I_2 back into I^-	Nat. Commun. 2015, 6, 10030
RT for 12 hours	methylamine	D	eliminate the remnant I_2 in the oxidized precursors by disproportionation	Adv. Mater. 2017, 29, 1606774
RT for 39 days	ITIC-Th	E	stabilize the $[PbI_6]^{4-}$ framework and suppress the yellow non-perovskite phase	Adv. Energy Mater. 2018, 8, 1703399
RT for 5 days	tri-iodide ions	D	compensates the loss of I^- ions due to the photo-oxidation, suppress the aggregation of colloids particles	Electrochimica Acta 2019, 311, 132-140
60 ℃ for 8 days	elemental sulfur	A	prevent the deprotonation of MAI to volatile methylamine and prevent the generation of δ-$FAPbI_3$	Adv. Energy Mater. 2019, 9, 1803476
RT for 230 days	KI+KI_3	A	form MAI_3 complex and maintain the amount of MA cations in precursor solution	Nano Energy 2019, 63, 103853
60 ℃ for 1 day	triethyl borate	A	restrain the deprotonation of MAI	Chem 2020, 6, 1369-1378
RT for 30 days	18C6	E	form complex with Pb^{2+} and suppress the formation of PbI_2 and δ-$FAPbI_3$	Adv. Funct. Mater. 2020, 30, 1908613
RT in air for 7 days	(hexafluoroisopropylidene)diphthalic anhydride	B	stabilize highly active Pb^{2+} and FA^+ ions by donating lone pair electrons	ACS Energy Lett. 2021, 6, 3425-3434
4 ℃ for 115 days	cold storage	AB	suppress the deprotonation of methylammonium, and the subsequent formation of MFA and DMFA	ChemSusChem 2021, 14, 2537-2546
60 ℃ for 7 days	phenylboric acid	AB	restrict the deprotonation of FAI and inhibit the self-condensation reaction to form s-triazine	Sol. RRL 2021, 5, 2000715
RT for 7 days	CsI	AB	coordinate methylamine and suppress the formation of the new species MFA and DMFA	Cell Rep. Phys. Sci. 2021, 2, 100432
RT for 60 days	benzylhydrazine hydrochloride	D	reduce the detrimental I_2 back to I^-	Sci. Adv. 2021, 7, eabe8130
50 ℃ for 5 days	H_3BO_3 additive	AB	inhibit the deprotonation of methylamine iodide and the transimine reaction of methylamine and formamidine iodide	SCIENTIA SINICA Chimica 2022(2), 52, 355-361
RT for 21 days	perovskite microcrystals	AB	protect the FA group and inhibit its adverse reaction with MA	ACS Appl. Mater. Interfaces 2022, 14, 52960-52970
RT in air for 50 days	diethyl (hydroxymethyl) phosphonate	ABD	inhibit the reactivity of the iodide and formamidinium ions	Adv. Energy Mater. 2022, 12, 2200650
30 ℃ for 60 days	formaldehyde	A	eliminate organoamines in the precursor	ACS Energy Lett. 2022, 7, 481-489
RT for 75 days	3-hydrazinobenzoic acid	ABD	suppress the oxidation of I^-, inhibit the deprotonation of organic cations and subsequent amine cation reaction	Angew. Chem. Int. Ed. 2022, 61, e202206914
RT for 21 days	triethyl phosphate	AB	prevent the deprotonation of MAI and inhibit the formation of MFA^+	Angew. Chem. Int. Ed. 2023, 62, e202215799
85 ℃ for 20 days	potassium formate	D	reduce I_2 back to I^-	Adv. Funct. Mater. 2023, 2303225

617

Table S8. Lifetimes of perovskite films obtained from TRPL spectra.

1.56 eV PVK	A_1	t_1 (ns)	A_2	t_2 (ns)	t_{ave} (ns)
W/O fresh	157.6	150.8	718.3	1411.0	1382.1
W/O 120 days	54.9	31.0	338.5	119.7	116.1
A18C6 fresh	68.9	218.0	848.4	5649.0	5632.0
A18C6 120 days	431.0	161.6	472.7	977.6	870.7

The fitting of lifetime follows the formula: $y = A_1*\exp(-x/t_1) + A_2*\exp(-x/t_2) + y_0$ where A is amplitude, t is a time constant.

Table S9. Lifetimes of perovskite films obtained from TRPL spectra.

1.56 eV	A_1	t_1 (ns)	A_2	t_2 (ns)	t_{ave} (ns)
W/O	157.6	150.8	718.3	1411.0	1382.1
A18C6	68.9	218.0	848.4	5649.0	5632.0
DA18C6	82.7	141.0	859.2	4989.9	4976.7
A15C5	93.3	352.4	834.8	3411.6	3376.7
DA15C5	236.7	460.7	638.1	3465.3	3324.1

Table S10. Parameters of dark *J-V* curves of perovskite films.

The defect densities (N_t) are determined according to the equation:

$$N_t = 2V_{TFL}\varepsilon_r\varepsilon_0 / (ed^2) \quad \text{(Equation 17)}$$

where ε_0 is the vacuum permittivity, ε_r is the relative dielectric constant, V_{TFL} represents the trap-filled limit voltage, e is the elementary charge, and d is the perovskite film thickness, respectively. (ε_0=8.854×10^{-12} F/m ε_r=47 e=1.602×10^{-19} C d=700 nm)

		W/O	A18C6	DA18C6	A15C5	DA15C5
electron	V_{TFL} (V)	0.93	0.61	0.62	0.81	0.82
	defect density (10^{15} cm^{-3})	9.9	6.5	6.6	8.6	8.7
hole	V_{TFL} (V)	0.89	0.6	0.58	0.67	0.73
	defect density (10^{15} cm^{-3})	9.4	6.4	6.1	7.1	7.7

Table S11. Average photovoltaic parameters of PSCs without and with ACEs under reverse scan.

	V_{oc} (V)	J_{sc} (mA cm^{-2})	FF (%)	PCE (%)
W/O	1.07±0.01	24.8±0.2	78.5±1.4	20.6±0.6
A18C6	1.17±0.01	24.7±0.3	81.6±0.6	23.5±0.5
DA18C6	1.15±0.01	24.9±0.4	80.7±0.7	23.2±0.6
A15C5	1.09±0.01	25.1±0.2	80.7±0.5	22.0±0.5
DA15C5	1.08±0.02	24.6±0.2	80.7±1.0	21.6±0.3

References

1 M. I. Saidaminov, A. L. Abdelhady, G. Maculan and O. M. Bakr, *Chemical communications*, 2015, **51**, 17658–17661.

2 M. I. Saidaminov, A. L. Abdelhady, B. Murali, E. Alarousu, V. M. Burlakov, W. Peng, I. Dursun, L. Wang, Y. He and G. Maculan, *Nature communications*, 2015, **6**, 7586.

3 N. J. Jeon, H. Na, E. H. Jung, T.-Y. Yang, Y. G. Lee, G. Kim, H.-W. Shin, S. Il Seok, J. Lee and J. Seo, *Nature Energy*, 2018, **3**, 682–689.

4 J. Xu, C. C. Boyd, Z. J. Yu, A. F. Palmstrom, D. J. Witter, B. W. Larson, R. M. France, J. Werner, S. P. Harvey and E. J. Wolf, *Science*, 2020, **367**, 1097–1104.

5 Y. Zhang, S. Seo, S. Y. Lim, Y. Kim, S.-G. Kim, D.-K. Lee, S.-H. Lee, H. Shin, H. Cheong and N.-G. Park, *ACS Energy Letters*, 2019, **5**, 360–366.

6 T. Lu and F. Chen, *Journal of computational chemistry*, 2012, **33**, 580–592.

7 G. Kresse and J. Furthmüller, *Physical review B*, 1996, **54**, 11169.

8 J. P. Perdew, K. Burke and M. Ernzerhof, *Physical review letters*, 1996, **77**, 3865.

9 D. A. Egger and L. Kronik, *The journal of physical chemistry letters*, 2014, **5**, 2728–2733.

10 S. Grimme, S. Ehrlich and L. Goerigk, *Journal of computational chemistry*, 2011, **32**, 1456–1465.

11 V. Wang, N. Xu, J.-C. Liu, G. Tang and W.-T. Geng, *Computer Physics Communications*, 2021, **267**, 108033.

12 D. J. Cram and J. M. Cram, *Science*, 1974, **183**, 803–809.

13 H.-R. Yu, J.-Q. Hu, X.-H. Lu, X.-J. Ju, Z. Liu, R. Xie, W. Wang and L.-Y. Chu, *The Journal of Physical Chemistry B*, 2015, **119**, 1696–1705.

14 Y. Zhang, Z. Xing, B. Fan, Z. Ni, F. Wang, X. Hu and Y. Chen, *Angewandte Chemie*, 2023, **135**, e202215799.

15 J. Kim, B. Park, J. Baek, J. S. Yun, H.-W. Kwon, J. Seidel, H. Min, S. Coelho, S. Lim and S. Huang, *Journal of the American Chemical Society*, 2020, **142**, 6251–6260.

16 D. P. McMeekin, Z. Wang, W. Rehman, F. Pulvirenti, J. B. Patel, N. K. Noel, M. B. Johnston, S. R. Marder, L. M. Herz and H. J. Snaith, *Advanced Materials*, 2017, **29**, 1607039.

17 K. Yan, M. Long, T. Zhang, Z. Wei, H. Chen, S. Yang and J. Xu, *Journal of the American Chemical Society*, 2015, **137**, 4460–4468.

18 J. C. Hamill Jr, J. Schwartz and Y.-L. Loo, *ACS Energy Letters*, 2017, **3**, 92–97.

19 B. Li, Q. Dai, S. Yun and J. Tian, *Journal of Materials Chemistry A*, 2021, **9**, 6732–6748.

20 M. Shamsipur and H. R. Pouretedal, *Journal of solution chemistry*, 1999, **28**, 1187–1205.

21 G. S. Shin, Y. Zhang and N.-G. Park, *ACS applied materials & interfaces*, 2020, **12**, 15167–15174.

22 C. Chen, Y. Rao, Z. Li, X. Wang, G. Cui, W. Wang and S. Pang, *Solar RRL*, 2021, **5**, 2000715.

23 M. Li, H. Li, Q. Zhuang, D. He, B. Liu, C. Chen, B. Zhang, T. Pauporté, Z. Zang and J. Chen, *Angewandte Chemie International Edition*, 2022, **61**, e202206914.

24 N. K. Noel, M. Congiu, A. J. Ramadan, S. Fearn, D. P. McMeekin, J. B. Patel, M. B. Johnston, B. Wenger and H. J. Snaith, *Joule*, 2017, **1**, 328–343.

25 S. Wang, Y. Jiang, E. J. Juarez-Perez, L. K. Ono and Y. Qi, *Nature Energy*, 2016, **2**, 1–8.

26 V. Valenzano, A. Cesari, F. Balzano, A. Milella, F. Fracassi, A. Listorti, G. Gigli, A. Rizzo, G. Uccello-Barretta and S. Colella, *Cell Reports Physical Science*.

27 J. Liang, X. Hu, C. Wang, C. Liang, C. Chen, M. Xiao, J. Li, C. Tao, G. Xing and R. Yu, *Joule*, 2022, **6**, 816–833.

28 M.-H. Li, J.-Y. Shao, Y. Jiang, F.-Z. Qiu, S. Wang, J. Zhang, G. Han, J. Tang, F. Wang and Z. Wei, *Angewandte Chemie*, 2021, **133**, 16524–16529.

29 S.-C. Liu, Z. Li, Y. Yang, X. Wang, Y.-X. Chen, D.-J. Xue and J.-S. Hu, *Journal of the American Chemical Society*, 2019, **141**, 18075–18082.

30 M. I. Saidaminov, A. L. Abdelhady, G. Maculan and O. M. Bakr, *Chemical communications*, 2015, **51**, 17658–17661.

31 Y. Jiang, S.-C. Yang, Q. Jeangros, S. Pisoni, T. Moser, S. Buecheler, A. N. Tiwari and F. Fu, *Joule*, 2020, **4**, 1087–1103.

32 Y. Shen, K. Deng, Q. Chen, G. Gao and L. Li, *Advanced Materials*, 2022, **34**, 2200978.

33 Z. Wan, H. Lu, J. Yang, Y. Zhang, F. Lin, J. Xia, X. Yao, J. Luo and C. Jia, *Journal of Energy Chemistry*, 2022, **74**, 489–496.

34 P. Gao, Y. Ji, J. Song, G. Zhou, J. Lai, X. Yin, Y. Li, T. Song, Z. Zhao, Q. Chen, W. Feng, L. Chen, Y. Zhang, S. Yang, B. Sun and F. Liu, *Cell Reports Physical Science*, 2021, **2**, 100450.

35 S. Ju Kim, R. Kumar Chitumalla, J.-M. Kim, J. Jang, J.-W. Oh, J. V. Milić and J.-Y. Seo, *Helvetica Chimica Acta*, 2023, **106**, e202200193.

36 R. Chen, Y. Wu, Y. Wang, R. Xu, R. He, Y. Fan, X. Huang, J. Yin, B. Wu and J. Li, *Advanced Functional Materials*, 2021, **31**, 2008760.

37 X. Wu, Y. Jiang, C. Chen, J. Guo, X. Kong, Y. Feng, S. Wu, X. Gao, X. Lu and Q. Wang, *Advanced Functional Materials*, 2020, **30**, 1908613.

38 X. Kong, Y. Jiang, Z. Li, Y. Zhou, Z. Xu, C. Cong, X. Gao, X. Lu, G. Zhou and J.-M. Liu, *Solar RRL*, 2021, **5**, 2000646.

39 K.-W. Huang, M.-H. Li, P.-T. Hsieh, C.-F. Lin, R. Rajendran, Y.-L. Tung and P. Chen, *J. Mater. Chem. C*, 2022, **10**, 16016–16027.

40 T.-S. Su, F. T. Eickemeyer, M. A. Hope, F. Jahanbakhshi, M. Mladenovic, J. Li, Z. Zhou, A. Mishra, J.-H. Yum and D. Ren, *Journal of the American Chemical Society*, 2020, **142**, 19980–19991.

41 H. Zhang, F. T. Eickemeyer, Z. Zhou, M. Mladenović, F. Jahanbakhshi, L. Merten, A. Hinderhofer, M. A. Hope, O. Ouellette and A. Mishra, *Nature Communications*, 2021, **12**, 3383.

42 X. Sun, F. Deng, S. Li, Y. Li, X. Lv, Y.-Z. Zheng and X. Tao, *Solar RRL*, 2022, **6**, 2200303.

43 P. W. Ayers, R. G. Parr and R. G. Pearson, *The Journal of chemical physics*.
44 M. A. Hossain, J. Jewaratnam, A. Ramalingam, J. N. Sahu and P. Ganesan, *Fuel*, 2018, **212**, 49–60.